SPE-193931-MS

A Geomechanics-Coupled Embedded Discrete Fracture Model and its Application in Geothermal Reservoir Simulation

Xiangyu Yu, Philip Winterfeld, Shihao Wang, Cong Wang, Lei Wang, and Yu-shu Wu, Colorado School of Mines

This paper was prepared for presentation at the SPE Reservoir Simulation Conference held in Galveston, Texas, USA, 10–11 April 2019.

Abstract

Geomechanics plays an essential role in fluid/heat flow by affecting hydraulic parameters. This influence could be amplified when fractures exist in the system because fracture aperture is highly sensitive to stresses. Coupled fluid/heat flow and geomechanics model is considerably important in simulating thermal-hydrologic-mechanical process, such as geothermal reservoir development. At the same time, due to the rock matrix shrinkage or expansion, thermal stress exerted on fracture surface remolds the aperture significantly and should be incorporated in modeling heat related process.

In this study, a coupled fluid/heat flow and geomechanics model, TOUGH2-THM, was developed based on the parallel framework of TOUGH2-CSM, with stress tensor components as primary variables. This modification is aiming on computing normal stresses on discrete fracture surface such that fracture related parameters can be fully coupled with geomechanical model. Embedded discrete fracture model was also improved to be compatible with the geomechanical coupling. Both of TOUGH2-THM and modified EDFM were validated for further application.

A geothermal reservoir simulation is conducted by the newly developed model, demonstrating the capability of this program to perform coupled modeling. It is also concluded that geomechanics and especially temperature alteration induced stress could affect fluid/heat flow in fracture and rock matrix. Thus, production efficiency could be impacted as well. The thermal stress generated by temperature reduction could enhance the fracture permeability in orders of magnitude. Various scenarios of injection temperature were modeled and compared. It can be observed that geothermal reservoir development is negatively influenced by geomechanical (and thermal) effect on fractures. The coupled model is helpful to improve the simulation accuracy.

Introduction

Thermal-hydrologic-mechanical (THM) is a complex process faced by engineers in several practical fields, such as CO_2 sequestration, nuclear waste disposal, thermal oil recovery and enhanced geothermal systems (EGS). Coupled model of fluid flow, heat transfer and geomechanics has become an important technique to numerically simulate this THM process in engineering projects (Taron and Elsworth, 2009; Rutqvist, 2011; Rutqvist et al., 2002; Zhang et al., 2016). The coupled model considers mutual effects among these three

THM processes and provides an integrated framework for application in practices. Among these fields, EGS is achieved by injecting cold water into artificial fractures and producing the hot water for electricity generation. Artificial fractures in low-permeability or nonpermeable rock are dominant flow channels for injected water so that the overall efficiency of an EGS project highly relies on the conductivity of these fractures. Flow of cold water in hot rocks and fractures, combined with the geo-stress alteration induced by pore pressure and thermal stress, has formed a THM process in which a coupled model is essential (Kohl et al., 1995; Rutqvist et al., 2002; Taron and Elsworth, 2010).

Coupling geomechanics into fluid/heat flow model has engaged sufficient attention and advances were accomplished by contributions from researchers. Traditionally, displacement vectors at grid nodes are regarded as primary variables in a mechanical module where constitutive stress-strain relations are applied. Therefore, finite element method is a common option for space discretization in such modules, compared to finite difference or finite volume method in flow modules. Flow and geomechanics can be solved separately in two modules between which an interface code is established to transfer information (Settari and Walters, 2001; Rutqvist et al., 2002; Minkoff et al., 2003). For an instance, Rutqvist et al. (2002) combined two well-known softwares, TOUGH2 and FLAC3D, as flow and mechanical models respectively. Both Settari and Walters (2001) and Rutqvist et al. (2002) explained two coupling schemes: explicit coupling and iterative coupling. Explicit coupling updates hydraulic parameters, such as porosity and permeability, at the beginning of a time step for fluid/heat flow. Iterative coupling implements this update at Newton's iteration level instead. Either one of these two schemes has drawbacks: explicit method only works with a sufficiently small time step and a weak dependence of hydraulic parameters on geomechanics; iterative method may cost an impractical amount of computation time. Kim et al. (2009) integrated the two modules into one model but the solution processes of flow and geomechanics were still not simultaneous. They discussed the advantages and deficiencies of different solution strategies on their stability and efficiency, but it seemed that these strategies are not unconditionally stable for universal coupled modeling cases. Winterfeld and Wu (2016) developed a fully coupled fluid/heat flow and geomechanics model for THM processes simulation based on TOUGH2-MP, a parallel framework extended from TOUGH2 code. The geomechanical governing equation was constructed based on thermal- poro-elastic Navier equation so that mean stress can be selected as a primary variable in addition to pressure, saturation and temperature. Moreover, this approach employed the integral finite different method for discretization in solving stress equations, same as flow equations. This fully coupled model were successfully adopted by several studies on geothermal and tight gas/oil reservoir simulation (Xiong et al., 2013; Wang et al., 2015; Xiong et al., 2015; Wang et al., 2017).

Quite a number of models were proposed for fluid flow between fracture and matrix in naturally fractured reservoir: the classical double porosity model (Warren and Root, 1963; Kazemi, 1969), the Multiple-INteracting-Continua (MINC) model (Pruess, 1983) and the multiple continuum model (Wu, 2000; Wu et al., 2004). These models are adopted to describe a reservoir with densely and well-distributed fractures so that multiple continua (fracture and matrix) can be treated as a uniformly-distributed 'sugar cubes' or nested cubes. Later on, the occurrence of hydraulic fracturing technology motivated engineers and scientists to put forward a methodology to model these long and discrete hydraulic fractures. Discrete fracture model (DFM) (Kim and Deo, 2000; Karimi-Fard et al., 2003; Garipov et al., 2016) and embedded discrete fracture model (EDFM) (Lee et al., 2001; Li and Lee, 2006; Moinfar, 2013; Wang, 2018) were brought in to accurately capture the irregular shape and distribution of hydraulic fractures. EDFM embeds the fractures with arbitrary shapes and strikes into the reservoir grids without sacrificing the accuracy, which prevails over DFM where mesh grids are specially designed and refined to conform the shape of fractures. Recently, EDFM and MINC techniques were integrated to handle the tight gas and oil reservoirs where both discrete and natural fractures play important roles in conducting fluid flow (Ding et al., 2018). In geothermal reservoirs, artificial fractures are commonly long and discrete fractures connecting injection and production wells, thus EDFM becomes the preferred option and not much attention need to be paid on the naturally distributed dense fractures.

It has been observed that fracture hydraulic parameters are strongly dependent on stress, pore pressure and temperature in a wide range of investigations (Barton et al., 1985; Rutqvist et al., 2002; McDermott and Kolditz, 2006; Moinfar et al., 2013; Chen et al., 2015). Fracture permeability is proved to be a function of aperture which, on the other hand, is correlated with normal stress exerted on the fracture surface. Moinfar et al. (2013) suggested to consider the influence of normal stress on the permeability of embedded discrete fracture and noticed that dynamic discrete fracture permeability affects the cumulative oil production. However, they didn't couple any geomechanical module but only incorporated dynamic correlations. Rutqvist et al. (2002) correlated fracture aperture as a function of exponential of normal stress compared to that Chen et al. (2015) treated fracture permeability as a function of exponential of pore pressure change. Speaking of temperature effect, it was mentioned in McDermott and Kolditz (2006) that thermal stress expanded the fracture aperture, and similar result was predicted by Wang et al. (2016) where significant fracture permeability enhancement could be expected during cold water injection into fractured geothermal reservoirs. As can be seen, accurately handling the geomechanical effect on fracture establishes a solid basis for building up a coupled THM model.

In this study, we first developed a fully coupled fluid/heat flow and geomechanics model with stress tensor components as primary variables, based on the methodology of Winterfeld and Wu (2016). This is followed by building up an improved EDFM on the basis of Wang (2018), aiming to take geomechanical effect on discrete fractures into account. Using this package of coupled THM model and EDFM, we simulated a geothermal reservoir development and observed how geomechanics could affect the injection and production process. This paper will start from the approach of coupled THM model development and model validation, followed by the method of reconstructing EDFM and validation. Finally, a geothermal reservoir simulation case will be demonstrated, in which different scenarios of injection will be compared and discussed.

Coupled Model of Fluid/Heat Flow and Geomechanics

The coupled model in this study is built on the parallel framework of TOUGH2-CSM (Winterfeld and Wu, 2016), a coupled model of fluid/heat flow and geomechanics for THM process. The newly developed model will be called TOUGH2-THM hereinafter. TOUGH2-CSM is established on TOUGH2-MP (Zhang et al., 2001), a massively parallel version of TOUGH2, for conducting non-isothermal multi-phase multi-component fluid flow simulations. TOUGH2-CSM contains several modules for different scenarios of reservoir fluids, such as water/air two-component two-phase module, CO_2/NaCl/H_2O three-component three-phase module and water/air/tracer three-component two-phase module. We will focus on water/air module in this study for the geothermal reservoir simulation. In this section, governing equations, spatial and time discretization and numerical solution approach that are adopted will be introduced. The ultimate goal of developing TOUGH2-THM is to incorporate geomechanics of embedded discrete fracture, which will be explained later in the part of mechanical governing equations.

Mass and Energy Balance Governing Equations

Mass and energy are to be balanced when the system is solved and in general form, they can be expressed as equation (1):

$$\frac{d}{dt}M^k = -\nabla \cdot \overrightarrow{F^k} + q^k \tag{1}$$

In equation (1), M^k, $\overrightarrow{F^k}$ and Q^k represent accumulation term, flux term and sink/source term respectively. The mass accumulation term can be written as:

$$M^k = \phi \sum_\beta S_\beta \rho_\beta X_\beta^k \tag{2}$$

in which ϕ is the rock porosity, S_β is the saturation of phase β, X_β^k is the mass fraction of component k in phase β. On the other hand, the heat accumulation term is:

$$M^{NK+1} = (1-\phi)\rho_R C_R T + \phi \sum_\beta S_\beta \rho_\beta u_\beta \tag{3}$$

in which ρ_R and C_R is the rock density and rock specific heat, T is the temperature and u_β is the specific internal energy of phase β.

Advective mass flux of component k is summed over all phases:

$$\overrightarrow{F^k}\Big|_{adv} = \sum_\beta X_\beta^k \overrightarrow{F_\beta} \tag{4}$$

where phase fluxes are given by a multiphase Darcy's law:

$$\overrightarrow{F_\beta} = \rho_\beta \overrightarrow{u_\beta} = -k \frac{k_{r\beta}\rho_\beta}{\mu_\beta}\left(\nabla P_\beta - \rho_\beta \vec{g}\right) \tag{5}$$

In the phase flux equation, $\overrightarrow{u_\beta}$ is the Darcy velocity of phase β, k is the absolute permeability, $k_{r\beta}$ is the relative permeability of phase β, μ_β is viscosity of phase β, and the phase pressure is $P_\beta = P + P_{c\beta}$, in which P is usually gas pressure and $P_{c\beta}$ is the capillary pressure of phase β with respect to gas.

Heat flux is the sum of conductive and convective components:

$$\vec{F}^{NK+1} = -\lambda \nabla T + \sum_\beta h_\beta \overrightarrow{F_\beta} \tag{6}$$

where λ is the thermal conductivity and h_β is the specific enthalpy in phase β.

Mechanical Governing Equation

Mechanical equation starts from the linear elasticity, Hook's law, considering thermal and pore pressure effect:

$$\bar{\tau} - h(P,T)\bar{I} = 2G\bar{\varepsilon} + \lambda(tr\bar{\varepsilon})\bar{I} \tag{7}$$

in which $\bar{\tau}$ is the stress tensor and $\bar{\varepsilon}$ is the strain tensor which can be calculated by displacement vector $\vec{u}$, λ and G in equation (7)(7) are the Lame parameters, $\bar{I}$ is the unit matrix and $tr\bar{\varepsilon}$ is the trace of strain tensor. The thermal and pore pressure term is expressed as below:

$$h(P,T) = \alpha P + 3\beta K\left(T - T_{ref}\right) \tag{8}$$

in which α is Biot's coefficient, β is thermal expansion coefficient and K is the bulk modulus.

The static equilibrium states that stress tensor and body force, $\overline{F_b}$ should satisfy:

$$\nabla \cdot \bar{\tau} + \overline{F_b} = 0 \tag{9}$$

Combining equation (7) and (9) leads to the thermo-poro-elastic Navier equation:

$$\nabla[h(P,T)] + (\lambda + G)\nabla(\nabla \cdot \vec{u}) + G\nabla^2\vec{u} + \overline{F_b} = 0 \tag{10}$$

Taking the divergence of equation (10) should reach:

$$\nabla^2[h(P,T)] + (\lambda + 2G)\nabla^2(\nabla \cdot \vec{u}) + \nabla \cdot \overline{F_b} = 0 \tag{11}$$

Since the divergence of displacement vector, $\nabla \cdot \vec{u}$ can be related with volumetric strain, ε_v:

$$\nabla \cdot \vec{u} = \frac{\partial u_x}{\partial x} + \frac{\partial u_y}{\partial y} + \frac{\partial u_z}{\partial z} = \varepsilon_{xx} + \varepsilon_{yy} + \varepsilon_{zz} \tag{12}$$

in which ε_{xx}, ε_{yy} and ε_{zz} are the strains in x, y and z direction, u_x, u_y and u_z are displacements in x, y and z direction. Taking the trace of equation (7) gives:

$$K\varepsilon_v = \tau_m - h(P,T) \tag{13}$$

Combining equation (11) (12) (13) provides (Winterfeld and Wu, 2016):

$$\frac{3(1-\nu)}{1+\nu}\nabla^2\tau_m + \nabla \cdot \overline{F_b} - \frac{2(1-2\nu)}{1+\nu}\nabla^2[h(P,T)] = 0 \tag{14}$$

in which ν is Poisson's ratio. The form of this mean stress equation is much similar with equation (1) without accumulation term. This is the reason why TOUGH2-CSM selected mean stress as an additional primary variable and employed the same spatial discretization approach for solving the mean stress.

Winterfeld and Wu (2016) mentioned the formulations for the stress tensor components based on the components of equation (10):

$$\begin{aligned}\frac{\partial^2}{\partial x^2}[h(P,T)] + \frac{3}{2(1+\nu)}\frac{\partial^2}{\partial x^2}(\tau_m - h(P,T)) \\ + \frac{1}{2}\nabla^2\left(\tau_{xx} - h(P,T) - \frac{3\nu}{1+\nu}(\tau_m - h(P,T))\right) \\ + \frac{\partial}{\partial x}F_{b,x} = 0\end{aligned} \tag{15}$$

$$\begin{aligned}\frac{\partial^2}{\partial y^2}[h(P,T)] + \frac{3}{2(1+\nu)}\frac{\partial^2}{\partial y^2}(\tau_m - h(P,T)) \\ + \frac{1}{2}\nabla^2\left(\tau_{yy} - h(P,T) - \frac{3\nu}{1+\nu}(\tau_m - h(P,T))\right) \\ + \frac{\partial}{\partial y}F_{b,y} = 0\end{aligned} \tag{16}$$

$$\begin{aligned}\frac{\partial^2}{\partial z^2}[h(P,T)] + \frac{3}{2(1+\nu)}\frac{\partial^2}{\partial z^2}(\tau_m - h(P,T)) \\ + \frac{1}{2}\nabla^2\left(\tau_{zz} - h(P,T) - \frac{3\nu}{1+\nu}(\tau_m - h(P,T))\right) \\ + \frac{\partial}{\partial z}F_{b,z} = 0\end{aligned} \tag{17}$$

$$\begin{aligned}\frac{\partial^2}{\partial x \partial y}[h(P,T)] + \frac{3}{2(1+\nu)}\frac{\partial^2}{\partial x \partial y}(\tau_m - h(P,T)) + \frac{1}{2}\nabla^2\tau_{xy} \\ + \frac{1}{2}\left(\frac{\partial}{\partial x}F_{b,x} + \frac{\partial}{\partial y}F_{b,y}\right) = 0\end{aligned} \tag{18}$$

$$\frac{\partial^2}{\partial z\partial y}[h(P,T)] + \frac{3}{2(1+\nu)}\frac{\partial^2}{\partial z\partial y}(\tau_m - h(P,T)) + \frac{1}{2}\nabla^2\tau_{yz} + \frac{1}{2}(\frac{\partial}{\partial z}F_{b,z} + \frac{\partial}{\partial y}F_{b,y}) = 0 \tag{19}$$

$$\frac{\partial^2}{\partial x\partial z}[h(P,T)] + \frac{3}{2(1+\nu)}\frac{\partial^2}{\partial x\partial z}(\tau_m - h(P,T)) + \frac{1}{2}\nabla^2\tau_{xz} + \frac{1}{2}(\frac{\partial}{\partial x}F_{b,x} + \frac{\partial}{\partial z}F_{b,z}) = 0 \tag{20}$$

Equations (15)–(20) are the differential equations for stress components: τ_{xx}, τ_{yy}, τ_{zz}, τ_{xy}, τ_{yz}, τ_{xz}, known as Beltrami-Michell equations. As can be seen, these six components derived from equation (10) can also be regarded as governing equations and then the stress components can be solved during Newton iterations. TOUGH2-THM is designed to use pressure, saturation/mass fraction, temperature, mean stress, x-normal stress, y-normal stress, and three shear stresses as primary variables.

The main reason of making these modifications is the incorporation of EDFM. When embedded discrete fractures intersect with the reservoir grids, the normal stress on the fracture surface is of more concern on how the fluid flow in fractures would be affected. In our study, it is assumed that discrete fracture embedded in a reservoir grid has the same stress state with this grid block, enabling the normal stress to be obtained by stress transformation in three-dimensional space, using all stress tensor components. Embedded discrete fracture permeability is strongly dependent on normal stress, which could possibly impact the stability and accuracy of numerical solution if iterative or explicit coupling is adopted. In order to avoid this unfavorable condition, primary variable list is extended so that fracture porosity and permeability can be updated implicitly by normal stress.

Numerical Discretization for Space and Time

TOUGH2-THM discretizes the space and time using Integral Finite Difference (IFD) and fully-implicit backward Finite Difference (FD) method respectively. IFD approach ensures the local mass and energy conservation which governs the fluid and heat flow equations. The governing equation of geomechanics can be discretized by IFD as well. The general form of governing equation, derived from equation (1) by applying IFD, can be expressed as:

$$\frac{d}{dt}\int_{V_n} M^k dV_n = \int_{\Gamma_n} \overrightarrow{F^k}\cdot\vec{n}\,d\Gamma_n + \int_{V_n} q^k dV_n \tag{21}$$

in which, V_n is the volume of n^th^ grid block, Γ_n is the surface area of n^th^ grid block and $\vec{n}$ is the normal vector pointing outwards on the surface. A further step of discretizing equation (21) achieves:

$$\frac{d}{dt}\left(M_n^k V_{n,0}(1-\varepsilon_{v,n})\right) = \sum_m A_{nm,0}(1-\varepsilon_{A,nm})F_{nm}^k + q_n^k V_{n,0}(1-\varepsilon_{v,n}) \tag{22}$$

in which $V_{n,0}$ is the grid block area at zero strain, $A_{nm,0}$ is the contact area at zero strain between the nth grid block of interest and its neighbor, mth grid block, F_{nm}^k is the flux between nth grid block and mth grid block, $\varepsilon_{v,n}$ is the volumetric strain and $\varepsilon_{A,nm}$ is the weighted area strain, both calculated from x, y and z normal strains. The approach of IFD can be demonstrated by Figure 1.

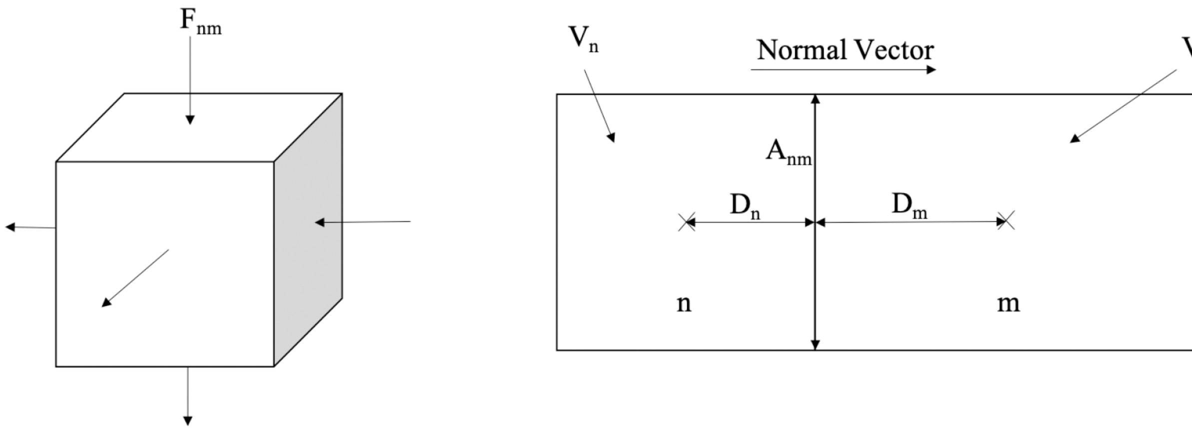

Figure 1—Discretized grid and its relationship with neighbors: demonstrating how flux flow in/out to the grid and flux between grid n and grid m

IFD approximates the advective mass flux for component k using Darcy's law, as shown in the following formulation:

$$\begin{aligned} &A_{nm}F_{nm}^{k} \\ &= \sum_{\beta} -k_{nm}\left(\frac{k_{r\beta}\rho_{\beta}X_{\beta}^{k}}{\mu_{\beta}}\right)_{nm}\left(\frac{P_n + P_{c\beta,n} - P_m - P_{c\beta,m}}{D_{n,0}\left(1-\varepsilon_{D,n}\right) + D_{m,0}\left(1-\varepsilon_{D,m}\right)}\right. \\ &\left. - \rho_{\beta,nm}g_{nm}\right)A_{nm,0}(1-\varepsilon_{A,nm}) \end{aligned} \tag{23}$$

in which $\varepsilon_{D,m}$ is the normal strain in the connection direction of mth grid block. Heat flux can also be computed by:

$$\begin{aligned} &A_{nm}F_{nm}^{NK+1} \\ &= -\lambda_{nm}(T_n - T_m)A_{nm,0}(1-\varepsilon_{A,nm}) \\ &+ \sum_{\beta} -k_{nm}\left(\frac{k_{r\beta}\rho_{\beta}X_{\beta}^{k}}{\mu_{\beta}}\right)_{nm}\left(\frac{P_n + P_{c\beta,n} - P_m - P_{c\beta,m}}{D_{n,0}\left(1-\varepsilon_{D,n}\right) + D_{m,0}\left(1-\varepsilon_{D,m}\right)}\right. \\ &\left. - \rho_{\beta,nm}g_{nm}\right)A_{nm,0}(1-\varepsilon_{A,nm})h_{\beta} \end{aligned} \tag{24}$$

in which, again, h_β is the specific enthalpy of phase β.

Discretization of stress equations is slightly different from flow and heat equations. Aiming to take heterogeneity into consideration, stress equations are discretized in a manner called flux and interface approach. This approach will be explained here by taking mean stress and x-direction normal stress as examples.

As was mentioned above, equation (14) governs the mean stress and can be written in the discretized form similar to equation (21) without accumulation term:

$$\int_{\Gamma_n} \overrightarrow{F^{NK+2}} \cdot \vec{n} d\Gamma_n = 0 \tag{25}$$

in which

$$\overrightarrow{F^{NK+2}} = \frac{3(1-\nu)}{1+\nu}\nabla\tau_m + \overrightarrow{F_b} - \frac{2(1-2\nu)}{1+\nu}\nabla[h(P,T)] \tag{26}$$

The mean stress flux is defined as:

$$\Psi_\tau = \frac{3(1-\nu)}{1+\nu}\nabla\tau_m + \overline{F_b} - \frac{2(1-2\nu)}{1+\nu}\nabla[h(P,T)] \tag{27}$$

As a result, there is a stress flux from nth grid to the contact interface, and a stress flux from interface to mth grid, which are defined as, Ψ_τ^- , and Ψ_τ^+ respectively along the normal vector direction. Ψ_τ^+, Ψ_τ^- can be computed using mth and nth grid properties as follows:

$$\Psi_{\tau,+} = \frac{3(1-\nu_+)}{1+\nu_+}\frac{\tau_{m,+}-\tau_{m,int}}{s_+} + \overline{F_{b,+}} - \frac{2(1-2\nu_+)}{1+\nu_+}\frac{h(P,T)_+ - h(P,T)_{+,int}}{s_+} \tag{28}$$

$$\Psi_{\tau,-} = \frac{3(1-\nu_-)}{1+\nu_-}\frac{\tau_{m,int}-\tau_{m,-}}{s_-} + \overline{F_{b,-}} - \frac{2(1-2\nu_-)}{1+\nu_-}\frac{h(P,T)_{int,-} - h(P,T)_-}{s_-} \tag{29}$$

where + and − represent mth and nth grids respectively and s_+ and s_- are used to replace D_m and D_n for a general description of two-grid connection. $h(P, T)_{int,+}$ and $h(P, T)_{int,-}$ are two thermal and pressure terms evaluated at two sides of the interface.

Equation (28) and (29) are combined to solve for $\tau_{m,int}$, under the condition of $\Psi_{\tau,+} = \Psi_{\tau,-} = \Psi_\tau$, resulting in:

$$\Psi_\tau = \frac{\left\{\begin{array}{c} \tau_{m,+} - \tau_{m,-} + \frac{s_+(1+\nu_+)}{3(1-\nu_+)}F_{b,+} + \frac{s_-(1+\nu_-)}{3(1-\nu_-)}F_{b,-} \\ -\frac{2(1-2\nu_+)}{3(1-\nu_+)}\left(h(P,T)_+ - h(P,T)_{+,int}\right) - \frac{2(1-2\nu_-)}{3(1-\nu_-)}\left(h(P,T)_{-,int} - h(P,T)_-\right) \end{array}\right\}}{\frac{s_+(1+\nu_+)}{3(1-\nu_+)} + \frac{s_-(1+\nu_-)}{3(1-\nu_-)}} \tag{30}$$

$$\tau_{m,int} = \tau_{m,+} - \frac{s_+(1+\nu_+)}{3(1-\nu_+)}\left(\Psi_\tau - \overline{F_{b,+}} + \frac{2(1-2\nu_+)}{1+\nu_+}\frac{h(P,T)_+ - h(P,T)_{+,int}}{s_+}\right) \tag{31}$$

where $\tau_{m,int}$ is the mean stress at the interface. After the derivation using flux and interface approach, equation (25) becomes:

$$\sum_m A_{nm,0}(1-\varepsilon_{A,nm})\Psi_{\tau,nm} = 0 \tag{32}$$

in which the distance from the center to the interface is calculated by considering normal strain.

Normal stresses and shear stresses can be discretized as well by the same approach from equation (15). Examples below are shown for x-direction normal stress only and the other stresses share similar formulations:

$$\Psi_{xx} = \frac{\left\{\begin{array}{c} \tau_{xx,+} - \tau_{xx,-} \\ +2s_+F_{b,x+} + 2s_-F_{b,x-} - \frac{3\nu_+}{1+\nu_+}\left(\tau_{m,+} - \tau_{m,int}\right) - \frac{3\nu_-}{1+\nu_-}\left(\tau_{m,int} - \tau_{m,-}\right) \\ +\frac{3s_+}{1+\nu_+}\frac{\tau_{m,+} - \tau_{m,int}}{x_+} + \frac{3s_-}{1+\nu_-}\frac{\tau_{m,int} - \tau_{m,-}}{x_-} \\ +\frac{2\nu_+ - 1}{1-\nu_+}\left(h(P,T)_+ - h(P,T)_{+,int}\right) + s_+\frac{2\nu_+ - 1}{1-\nu_+}\frac{h(P,T)_+ - h(P,T)_{+,int}}{x_+} \\ +\frac{2\nu_- - 1}{1-\nu_-}\left(h(P,T)_{-,int} - h(P,T)_-\right) + s_-\frac{2\nu_- - 1}{1-\nu_-}\frac{h(P,T)_{-,int} - h(P,T)_-}{x_-} \end{array}\right\}}{\frac{s_+(1+\nu_+)}{3(1-\nu_+)} + \frac{s_-(1+\nu_-)}{3(1-\nu_-)}} \tag{33}$$

where x_+ and x_- terms exist only when x-direction connections are under calculation, otherwise the related terms are regarded as zero. Equation (33) illustrates that interface mean stress facilitates the computation of x-direction normal stress flux and so does interface pressure and temperature. In TOUGH2-CSM and TOUGH2-THM, interface quantities are updated at each Newton iteration level by equation (30) and (31) for stress flux assemblage.

Numerical Solution Approach

This non-linear system can be solved fully implicitly in time after spatial discretization, by the approach known as Newton's method. The program iterates to compute residual equation within a timestep until convergence when residual is small enough. The residual equation can be written as:

$$\begin{aligned} R_n^{k,i+1} = {} & \left(M_n^k\left(1-\varepsilon_{v,n}\right)\right)^{i+1} - \left(M_n^k\left(1-\varepsilon_{v,n}\right)\right)^{i} \\ & - \Delta t \sum_m \left(\frac{A_{nm,0}}{V_{n,0}}\left(1-\varepsilon_{A,nm}\right)F_{nm}^k\right)^{i+1} \\ & - \Delta t \left(q_n^k\left(1-\varepsilon_{v,n}\right)\right)^{i+1} \end{aligned} \tag{34}$$

in which, k represents the index of governing equations of nth grid block, $i + 1$ and i represent the new and old time steps. The objective of Newton's method is reducing residual of each governing equation of each grid block to zero. By the definition of Taylor's theory:

$$R_n^{k,p+1}\left(x_{l,p+1}\right) = R_n^{k,p+1}\left(x_{l,p}\right) + \sum_l \frac{\partial R_n^{k,p+1}}{\partial x_l}\Big|_p \left(x_{l,p+1} - x_{l,p}\right) \tag{35}$$

in which l is the index of primary variable and p is the iteration level. In order to make equation (35) to be zero, the following needs to be satisfied:

$$-\sum_l \frac{\partial R_n^{k,p+1}}{\partial x_l}\Big|_p \left(x_{l,p+1} - x_{l,p}\right) = R_n^{k,p+1}\left(x_{l,p}\right) \tag{36}$$

where the left-hand-side derivative terms, evaluated by numerical differentiation, constitute Jacobian matrix. Equation (36) builds up the discretized linear system of equations and the increments of primary variables will be solved for the next iteration. During each iteration, secondary variables, such as porosity, permeability, strain, fluid density and specific enthalpy, viscosity, relative permeability are updated by primary variables.

Parallel Framework and Program Structure

TOUGH2-THM is developed based on a parallel framework of TOUGH2-MP. The program relies on Message Passing Interface (MPI) for parallel implementation, run as multiple processes on multiple processors simultaneously. When performing parallel computation, TOUGH2-MP code partitions the reservoir domain into sub-domains using the partitioning algorithm from METIS software package (Karypis and Kumar, 1998). The subdomains are handled by processors for computing secondary thermophysical properties, assembling mass, energy and stress residual equations and building local Jacobian linear systems. Local systems are solved in parallel by multiple processors through AZTEC linear solver package. Information is exchanged during each iteration for assembling Jacobian matrix and also for solving the linear equations (Zhang et al., 2001). Parallel simulation enables users to model a large-scale problem with a significant number of grids efficiently and practically. In this study, due to the extension of primary variable list, parallel computation would help to mitigate the increased burden of solving large linear systems of equations. In this section, the parallel structure and overall program structure will be briefly introduced, but the parallel performance will not a focus in this paper.

Grid Partitioning for Parallel Simulation

In TOUGH family code, all grid blocks are given specific names (or indices) that are used for setting up connection data. Assembling mass, energy and mechanical equations for a grid block needs the primary and secondary parameters of all its connected neighbors even after partitioning assigned subdomains of grid blocks to different processors. Therefore, each of the processors is required to have access to the grids blocks that are directly connected to the border of this subdomain. TOUGH2-MP, after partition, divides the subdomain into three sets of grids: internal, border and external. This approach can be illustrated by Figure 2. The grids in red box has been assigned to the current processor and global indices (before partitioning) are shown in (a). This processor is connected to other four processors that contains neighbors of the current processor. Partitioning process assigns local indices to these grids in the red box from 1 to 16. The grids in green box are called internal sets which don't need any data from outside; the grids between green box and red box are called border sets which connects to the external sets.

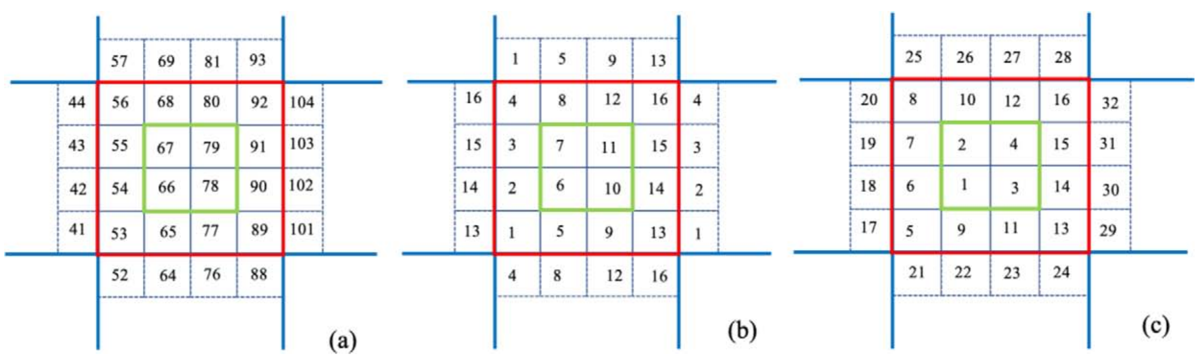

Figure 2—Grid indices before and after domain partition: (a) global indices before partition; (b) local indices after partition; (c) local indices after dividing into three sets

Local indices are first assigned in an ascending global index order, to each of the three sets. Then local connections are established using the local indices. Input parameters are distributed to different processors from the master processor according to global and local indices, global and local connections. External sets are prepared for data exchange between connected subdomains. After the local connection set up and data distributed, each processor should be able to conduct main computation. The overall structure of parallel processing is shown in Figure 3.

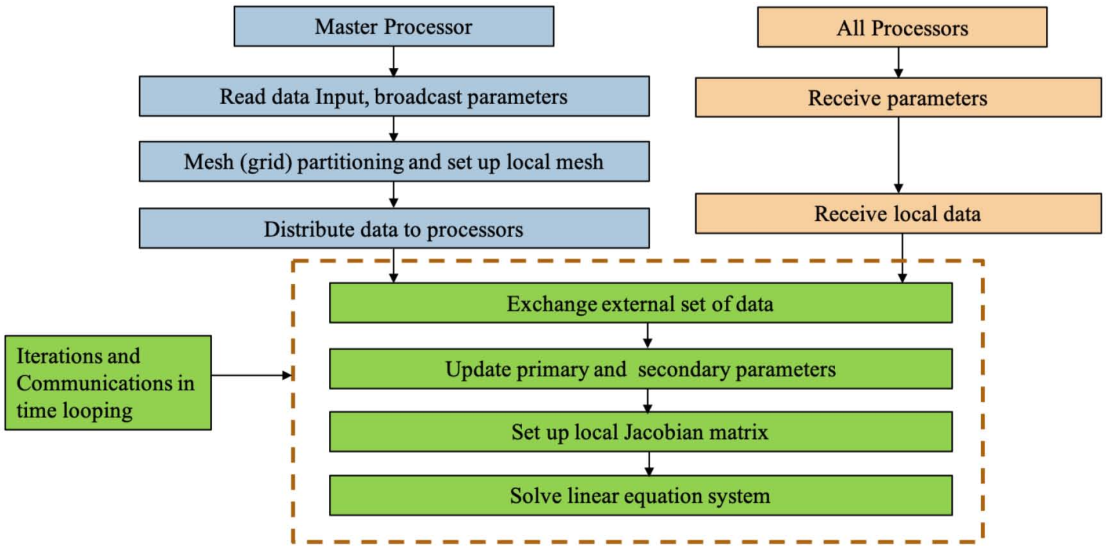

Figure 3—The structure of parallel processing for TOUGH2-THM

Computation and Program Structure

Each processor, in the main computation module, will initialize the stress, temperature and pore pressure first, by either equilibrium state computation or data input file. Then external and border data sets are exchanged for preparing time looping. Secondary variables are updated first based on primary variables from last iteration or time step. During Newton's iteration, mass, energy and stress equations are assembled, and Jacobian matrix is built for solution. Afterwards, AZTEC solver takes charge of solving local linear system for increment towards next iteration. Convergence will be checked when residual equations are computed and whether the system is converged determines the following step of entering next iteration or time step. The whole structure is illustrated in Figure 4.

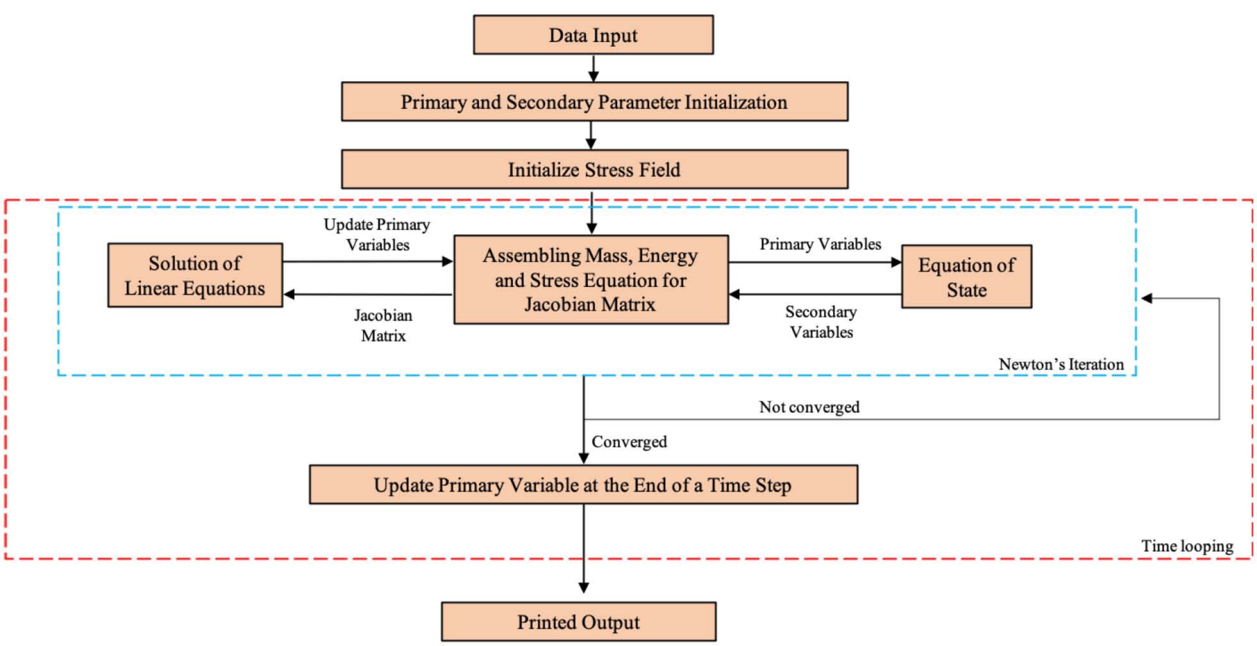

Figure 4—Program structure of the main computation (time looping and iteration)

It should be noted that exchanging data sets are time-consuming, reducing the efficiency of parallel performance. TOUGH2-MP exchanges only primary variables once for each iteration, using non-blocking communication. In this study, efficiency is sacrificed temporarily because the interface quantities are necessary for stress equation assembly. As is shown in shear stress equation (18)–(20), for the two connected grids of interest, cross derivative should be approximated by performing finite difference using stress and pressure on the block surface that may not be the current connection. Thus, it is possible that interface quantities of external grids are needed, which cannot be computed in the current processor. Consequently, this is a required data exchange procedure if no modification of local grid setup is desired.

Embedded Discrete Fracture Model

The concept of embedded discrete fracture is originally proposed by (Lee et al., 2001; Li and Lee, 2006) for modeling fluid flow between rock matrix and long fractures. Moinfar (2013) extended the model and applied it into three-dimensional compositional simulation. Wang (2018) developed an EDFM preprocessor in which arbitrary shape and strike of discrete fractures can be embedded into mesh grids. EDFM enables us to generate complex fracture geometry and model the fluid flow in fractured reservoirs. It is intuitive to treat the embedded discrete fracture as a well in its connected grid block and equation (22) becomes:

$$\frac{d}{dt}\left(M_n^k V_{n,0}\left(1-\varepsilon_{v,n}\right)\right) = \sum_m A_{nm,0}\left(1-\varepsilon_{A,nm}\right)F_{nm}^k + q_n^k V_{n,0}\left(1-\varepsilon_{v,n}\right) + q_{mf} \tag{37}$$

in which q_{mf} is the flow between discrete fracture and the connected matrix grid. This flow term can be computed by (Wang, 2018):

$$q_{mf} = FI\frac{\rho_\beta k k_{r\beta}}{\mu_\beta}\left(P_m - P_f + P_{cm} - P_{cf}\right) \tag{38}$$

Compared with Darcy's flow, FI is fracture index and should be expressed as $\frac{A}{D_m+D_f}$. Fracture index is used to describe the connection area and distance between fracture and matrix, similar with those between two normal grid blocks. EDFM is employing geometrical calculation to obtain such properties so that a set of new mesh beyond reservoir grids can be built. Wang (2018) regarded discrete fracture element as a grid block which has a relatively small volume and connections between fracture elements and Cartesian grid blocks are established for fluid/heat flow simulation. The improved model in this study is based on the program developed by Wang (2018). The principles of EDFM will be explained in this section, followed by the improvement of EDFM and geomechanical effect on embedded discrete fracture.

Geometrical Calculation of EDFM

EDFM approach is basically computing the intersection between an arbitrary plane and a box in three-dimensional space, which becomes a geometrical calculation problem. As shown in Figure 5, two planes in three-dimensional space intersect with a Cartesian grid block and with each other at the same time. Fracture plane has been cut into discrete pieces within this grid block, generating two fracture elements: red and green polygons. It is intuitive that the contact area between fracture element and the box is just the area of polygon and the contact area between two intersected fractures are fracture width multiplied by the length of line segment AB. Distance between a fracture element and a box can be calculated using (Li and Lee, 2006):

$$d_{fm} = \frac{\int \left(\frac{x_v}{V}\right) dV}{V} \tag{39}$$

in which x_v is the distance from an infinitesimal volume of the matrix grid box to the fracture plane. Such distance can be computed using Hessian form of the plane and the coordinate of the point:

$$\hat{n} \cdot \vec{x} = -p \tag{40}$$

$$D = \hat{n} \cdot \overrightarrow{x_0} + p \tag{41}$$

in which, $\hat{n}$ is the normal vector of the plane, $\overrightarrow{x_0}$ is the coordinate of the point and equation (40) is the Hessian form of a plane. The connection distance between two intersected fractures can be calculated by (Xu et al., 2017):

$$d_{ff} = \frac{\int_{S_1} x_n dS_1 + \int_{S_2} x_n dS_2}{S_1 + S_2} \tag{42}$$

where S_1 is the area of one part cut by the intersecting line segment and S_2 is the other, such as in Figure 5, red polygon is cut into two pieces by line segment AB. The distance from red fracture element to the interface AB is calculated by equation (42), similarly for green fracture element.

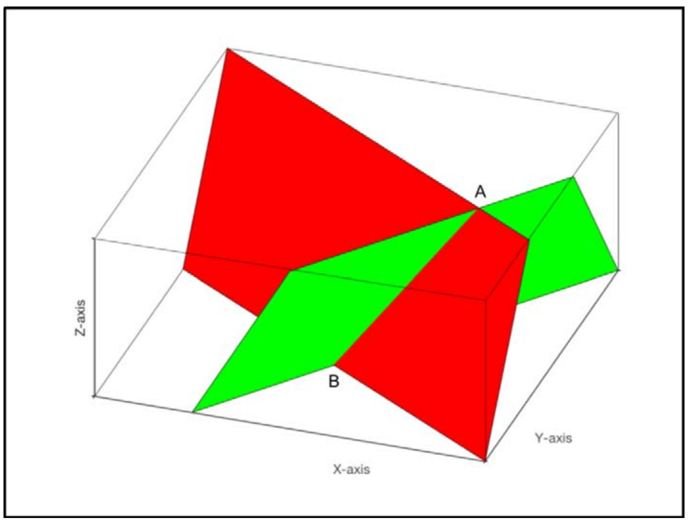

Figure 5—Two discrete fracture planes intersecting with a Cartisian grid block

The challenging task of establishing EDFM is to find the coordinates of the cut polygons, with which contact area and distance calculation above would not be an obstacle. Procedure proposed by Wang (2018) for box fracture intersection include:

1. Check if one or more of the polygon vertices is inside the box, save the vertex inside the box;
2. Check the intersection between box edge and fracture polygon and if intersection point is within polygon, save vertex if yes;
3. Check if polygon edge intersects with box face and if intersection point is within box face, save vertex if yes;
4. Check if any pair of the saved vertices is the same vertex and eliminate the duplicated vertex;
5. Sort vertices counter-clockwise and calculate discrete fracture area and contact distance.

The above procedure is performed between each fracture plane and grid box to locate all fracture elements. Wang (2018) integrated all fractures polygons into a single one within each Cartesian box. However, since it is desired to consider geomechanical effect on each discrete fracture polygon, EDFM was modified to treat fracture polygons individually. Hence, beyond the steps stated above, additional geometrical calculations are necessary:

6. Check if polygons are along the box surfaces, save these polygons for further use;
7. The Check polygon intersection on the connected face between two boxes, calculate contact area and distance if intersected;
8. Check polygon intersection on the connected edge between two boxes, calculate contact area and distance if intersected;
9. Eliminate duplicates of polygons along the box surfaces and check if intersected with polygons inside the box, calculate contact area and distance if yes.

The modification of fracture connection considers conditions illustrated in Figure 6. Although fractures intersected with each other could reach equilibrium due to high conductivity, this may not be true when geomechanics is taken into account or when grid box is large.

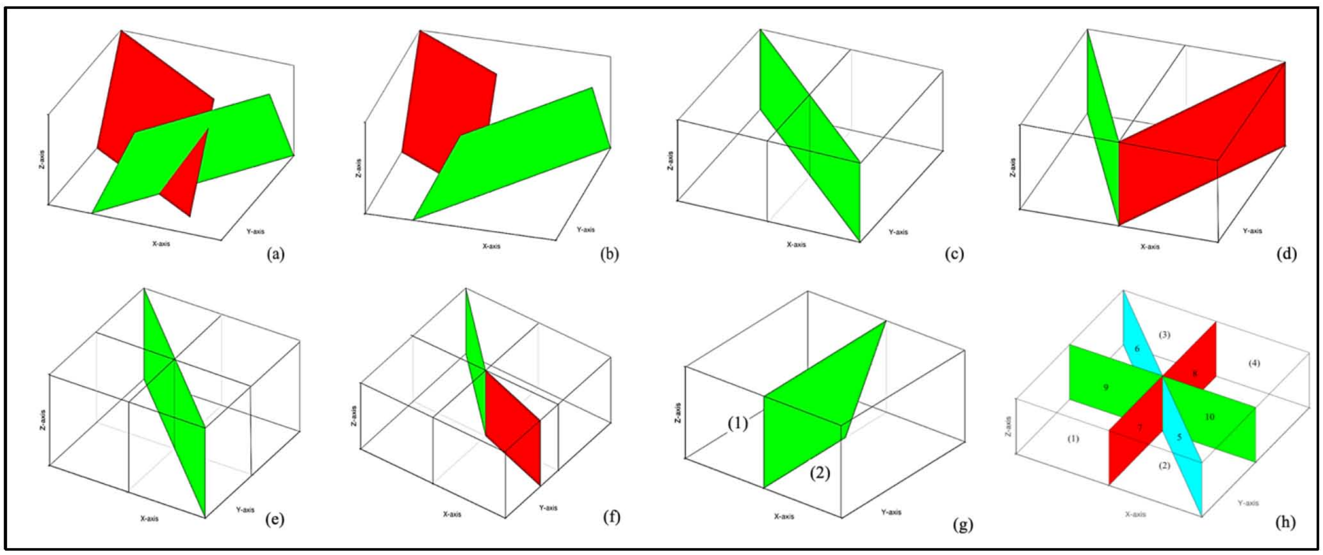

Figure 6—Fracture-fracture connection conditions considered by the modification of EDFM: (a) Partially intersection inside a box; (b) No intersection inside a box; (c) Connection on box faces; (d) Connection on edge of box faces; (e) Connection on box edges; (f) Connection of different fracture planes on box edges; (g) Polygons along box faces; (h) Connection between polygons along box faces and polygons inside boxes.

Geomechanical Effect on Embedded Discrete Fractrure and Rock Matrix

As mentioned in introduction section, discrete fracture permeability is a function of aperture whose change is highly dependent on effective normal stress exerted on the fracture surface. Barton et al. (1985) correlated fracture closure with normal stress:

$$\Delta b = \frac{\Delta \tau_n'}{k_n - \frac{\Delta \tau_n'}{\Delta b_{max}}} \tag{43}$$

in which Δb is the change of fracture aperture, Δb_{max} is the maximum closure and k_n is the fracture stiffness. Rutqvist et al. (2002) and Min et al. (2004) treated the fracture aperture as an exponential function of normal stress:

$$b = b_i + \Delta b = b_i + b_{max}(e^{-d\tau_n'} - e^{-d\tau_{ni}'}) \tag{44}$$

in which b is the current aperture under normal effective stress τ'_n, b_i is the initial aperture under the initial normal effective stress τ'_{ni}, b_{max} is the maximum aperture that can be reached, d is a coefficient measured by laboratory. Given the aperture of a fracture, fracture permeability can be calculated by:

$$k_f = \frac{b^2}{12b_i^2} k_i \tag{45}$$

in which k_f represents current permeability, k_i is the initial permeability of fracture. Similarly, porosity of fracture can be modeled by:

$$\phi_f = \frac{b}{12b_i} \phi_i \tag{46}$$

where ϕ_f is fracture porosity and ϕ_i is initial fracture porosity. Equations (44) (45) and (46) are adopted for modeling the geomechanical effect on fracture hydraulic parameters.

Hydraulic parameters of rock matrix are also correlated with stress or strain. The primary variables are mean stress, x-normal stress and y-normal stress, all of which are used to calculate the matrix grid block strain:

$$\tau_{zz} = 3\tau_m - \tau_{xx} - \tau_{yy} \tag{47}$$

where z-normal stress is treated as a secondary parameter (Jaeger et al., 2007),

$$\varepsilon_{xx} = \frac{1}{E}[\tau'_{xx} - \nu(\tau'_{yy} + \tau'_{zz})] \tag{48}$$

$$\varepsilon_{yy} = \frac{1}{E}[\tau'_{yy} - \nu(\tau'_{xx} + \tau'_{zz})] \tag{49}$$

$$\varepsilon_{zz} = \frac{1}{E}[\tau'_{zz} - \nu(\tau'_{xx} + \tau'_{yy})] \tag{50}$$

$$\varepsilon_v = \varepsilon_{xx} + \varepsilon_{yy} + \varepsilon_{zz} \tag{51}$$

in which ε_{xx}, ε_{yy} and ε_{zz} are normal strain along x, y and z directions, and ε_v is the volumetric strain which can also be calculated by equation (13). τ'_{xx}, τ'_{yy} and τ'_{zz} are effective normal stresses calculated by subtracting the thermal and pore pressure terms from total stresses, as shown in equation (7) and (8). Strains are affecting the contact distance and area between connected grid blocks:

$$D_n = D_{n,0} \frac{1 - \varepsilon_{nn}}{1 - \varepsilon_{nn,0}} \tag{52}$$

$$A_{nm} = \frac{1}{2} A_{nm,0} \left(\frac{1 - \varepsilon_{mn,1}}{1 - \varepsilon_{nn,1,0}} \frac{1 - \varepsilon_{mn,2}}{1 - \varepsilon_{nn,2,0}} + \frac{1 - \varepsilon_{mn,1}}{1 - \varepsilon_{mm,1,0}} \frac{1 - \varepsilon_{mm,1}}{1 - \varepsilon_{mm,1,0}} \right) \tag{53}$$

where nn represents direction of interest (xx, yy or zz), 1 and 2 in the subscript of strain are directions other than the direction of interest. Porosity can be calculated assuming that rock matrix solid compressibility is zero (Gutierrez et al., 2001):

$$\phi = 1 - \frac{1 - \phi_r}{\left(\frac{1 - \varepsilon_v}{1 - \varepsilon_{v,r}} \right)} \tag{54}$$

in which ϕ_r and $\varepsilon_{v,r}$ are residual porosity and volumetric strain. Equation (54) can be rewritten as:

$$\frac{1-\phi}{1-\phi_i} = \frac{1-\varepsilon_{v,i}}{1-\varepsilon_v} \tag{55}$$

through which current porosity can be calculated by initial ($\varepsilon_{v,i}$) and current volumetric strain. Permeability can be correlated with porosity (Rutqvist et al., 2002):

$$k = k_0 e^{c\left(\frac{\phi}{\phi_0}-1\right)} \tag{56}$$

where k_0 and ϕ_0 are initial or reference permeability and porosity of rock matrix.

As discussed above, it is assumed that during the solution process, embedded discrete fracture elements share the same stress state with the reservoir grid block (or interface stresses for fracture along the box surface). The assumption is made based on the fact that, within the large scale of reservoir, no shear displacement will occur on fracture surface and embedded fracture is treated as a continuum within rock matrix. Hence, normal stress on fracture surface becomes secondary parameters and can be calculated by stress transformation in three-dimensional space accordint to Jaeger et al. (2007):

$$\begin{aligned}\tau_{z'z'} = l_{31}^2\tau_{xx} + l_{32}^2\tau_{yy} + l_{33}^2\tau_{zz} + 2l_{31}l_{32}\tau_{xy} + 2l_{31}l_{33}\tau_{xz} \\ + 2l_{32}l_{33}\tau_{yz}\end{aligned} \tag{57}$$

where subscript $z'z'$ is the normal direction of fracture face after stress transformation, and l_{31}, l_{32} and l_{33} are related with the longitudinal (λ) and zenith angles (θ) of coordinate transformation:

$$l_{31} = \sin\theta\cos\lambda \ , l_{32} = \sin\theta\sin\lambda \ , l_{33} = \cos\theta \tag{58}$$

Longitudinal and zenith angles can be specified by the plane normal vector when generating EDFM mesh, and then transferred to coupled model for simulation. As can be seen in equation (57), normal stress on fracture is dependent on normal stress and shear stress of the matrix grid block. This explains, again, the reason why we would like to extend the primary variable list.

Normal stress on fracture face is a total stress without accounting for the pore pressure and thermal stresses yet. Wang et al. (2016) modeled fracture aperture change by computing the matrix displacement. McDermott and Kolditz (2006) pointed out that fracture face is being 'pulled' by rock matrix when temperature is reduced, and the thermal stress can be expressed by:

$$\tau_{thermal} = 3\beta_m K_m (T_f - T_{fi}) \tag{59}$$

in which β_m and K_m are expansion coefficient and bulk modulus of rock matrix grid but T_f and T_{fi} are current and initial temperatures of fracture element. Temperature reduction generates a negative (tensile) stress on the contact surface between matrix and surface, as shown in Figure 7. Normal effective stress on fracture surface now becomes:

$$\tau_n' = \tau_{z'z'} - \alpha_f P_f + \tau_{thermal} \tag{60}$$

Integration of equation (44) and (60) could capture the enhanced fracture permeability due to temperature changes.

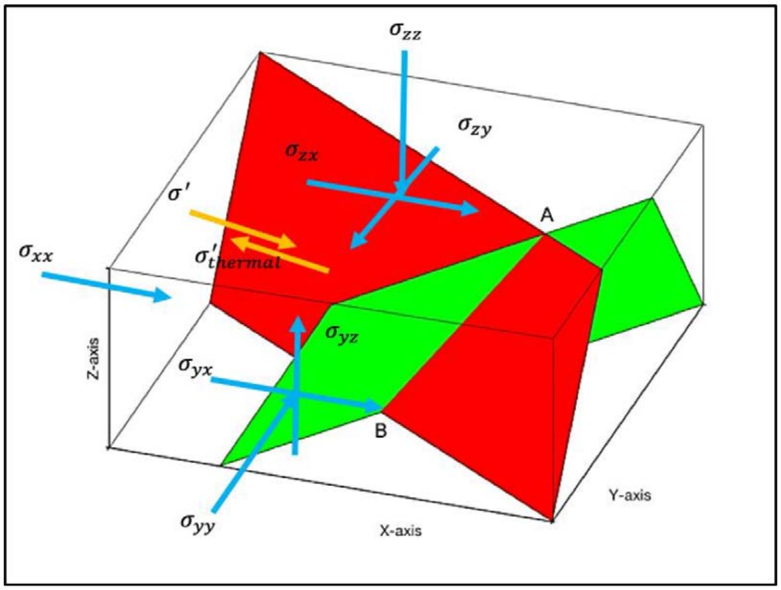

Figure 7—Normal stress and thermal stress on red fracture plane: yellow arrow points towards the direction of stress; blue arrows represent total stress of matrix grid block. Fracture red and green share the same stress state with the box but the stress transformation will provide different normal stresses for them.

Model Validation

In this section, EDFM and coupled fluid/heat flow and geomechanics model will be validated using existing model and analytical solutions.

Validation of EDFM

Wang (2018) has validated EDFM using analytical solution and Local Grid Refinement (LGR). Since EDFM in this work has been modified to explicitly include all discrete fracture elements. Validation should be performed for the newly developed program. Simulation result of LGR was compared with EDFM in this case. The reservoir model is shown in Figure 8 as a two-dimensional case including three fractures with intersections. LGR model had exactly the same geometrical parameters, except that near- fracture area was refined to capture the transient behavior of mass transfer between fracture and matrix. In total, EDFM had 2480 grids including matrix and fracture elements and LGR has 5325 grids. Dimension of the model was 100 m × 100 m × 20 m. Injection and production of water were both at fracture elements for 500 days. Input parameters for this case were shown in Table 1. Simulation was run on TOUGH2- THM without geomechanics coupling. EDFM took 55 seconds for computation and LGR took 3600 seconds due to the tiny dimension of fracture element. Simulation results are shown in Figure 9 and Figure 10. Note that flow rate in (b) of Figure 9 is the result of injecting cold water with 0.1 kg/s into a lower permeability reservoir for both EDFM and LGR approach, such that the transient rate can be prolonged for observation.

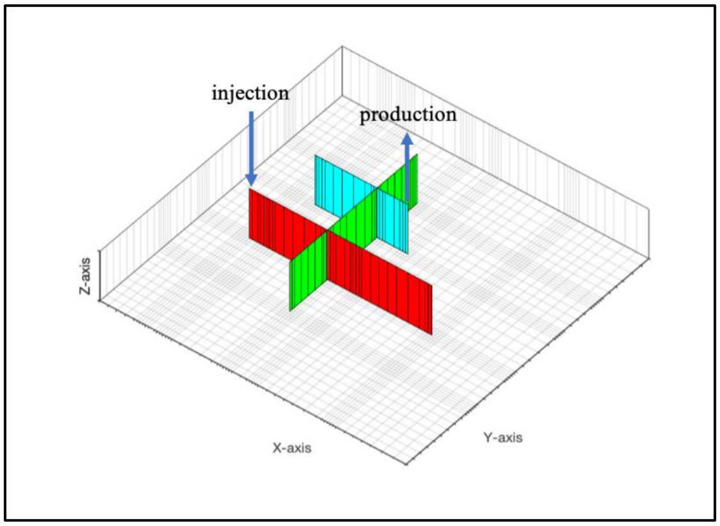

Figure 8—Geometrical models of validation case: three long fractures in a geothermal reservoir

Table 1—Input parameters for EDFM validation cases

Parameters	Value	Unit
Matrix Permeability	2e-14	m^2
Fracture Permeability	2e-11	m^2
Initial Reservoir Pressure	4.53e7	Pa
Initial Reservoir Temperature	300	°C
Production (constant pressure)	1e7	Pa
Injection (constant rate)	1	kg/s
Injection specific enthalpy	3e5	J/kg
Rock/Fracture Porosity	0.05	Unitless
Rock/Fracture Heat Conductivity	5	W/(m°C)
Rock/Fractue Specific Heat	1000	J/(kg°C)
Production Well Index	4e-10	m^3

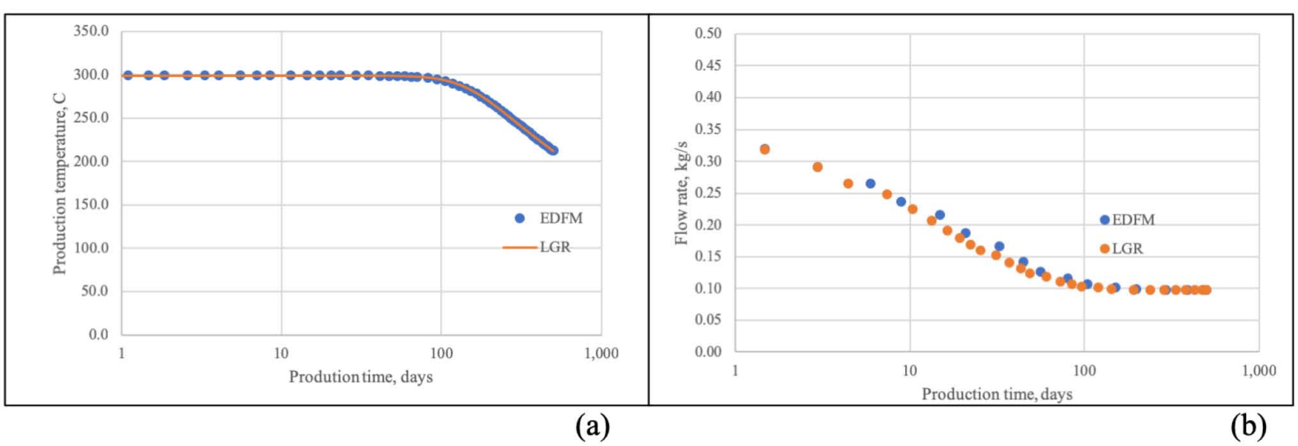

Figure 9—Comparison of (a) production temperature and (b) flow rate for LGR and EDFM cases (0.1 kg/s of injection for (b))

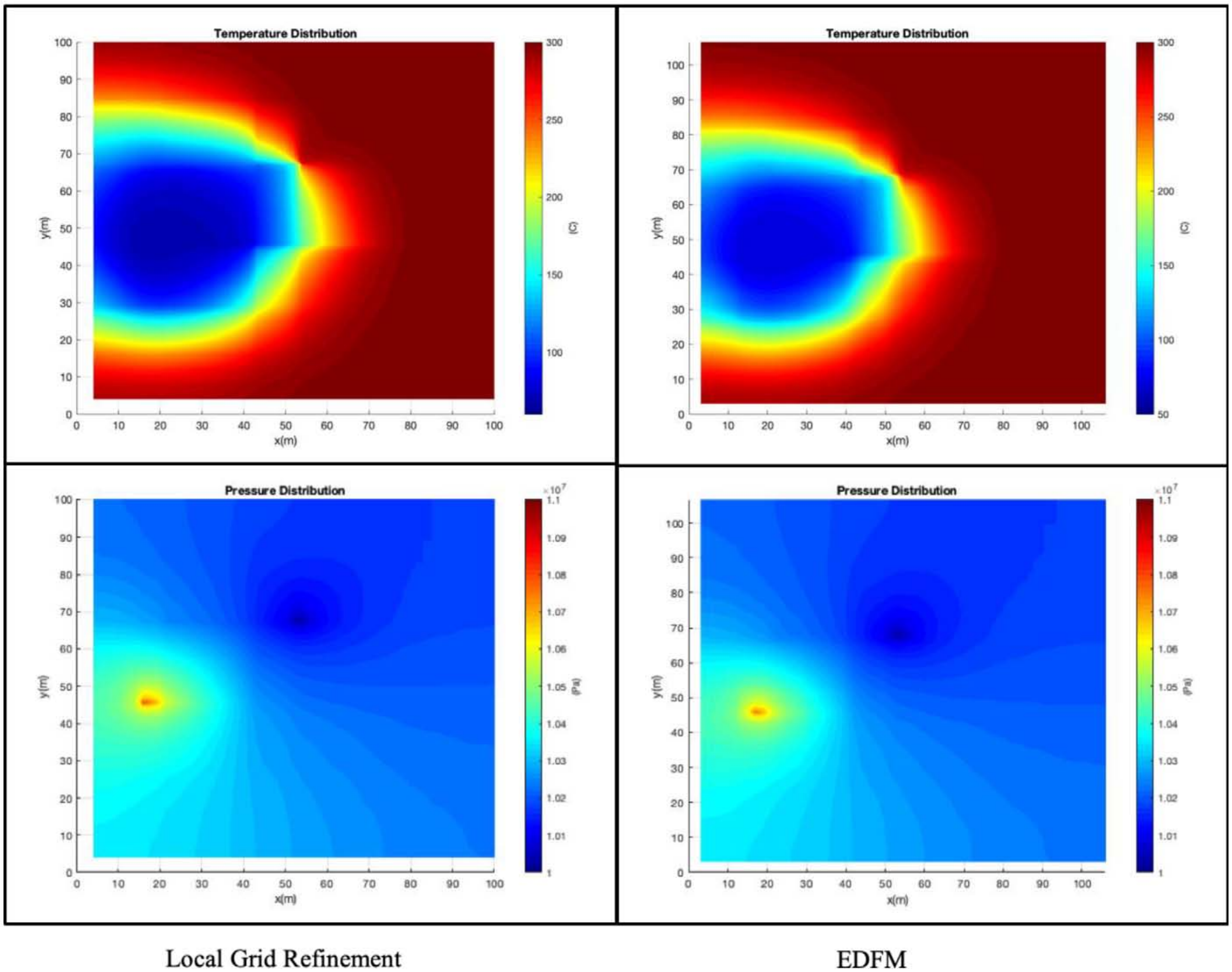

Figure 10—Comparison of temperature and pressure distribution after 500 days of injection for LGR and EDFM cases

It is shown in the comparison that simulation results of EDFM match well with those of LGR on pressure/temperature distribution, temperature production and transient flow rate. The matched results validate the accuracy of fluid/heat flow calculation of the modified model. Moreover, EDFM exhibits a better performance with much fewer grids and faster computation than LGR.

Validation of Fully Coupled Fluid/Heat Flow and Geomechanics Model

TOUGH2-THM computes all of the stress tensor components fully implicitly and fully coupled with fluid/heat flow. Compared with TOUGH2-CSM, the improvement mainly lies in solving normal stresses on arbitrarily-striked embedded discrete fractures. TOUGH2-CSM updates stress tensor for each grid block after a time step convergence and has been validated by analytical solution and existing modeling work. Thus, in order to validate this newly developed fully coupled model, it is desired to compare TOUGH2-THM with TOUGH2-CSM, and with analytical solution as well.

Comparision between TOUGH2-THM and TOUGH2-CSM. A coarse grid problem was built for comparing coupled modeling results of two programs: a homogeneous model of 10×10×4 grids with dimensions of 100 m×100 m×24 m. Grid blocks were all of 10 m×8 m× 6m, as shown in Figure 11. Injection of cold water into a hot geothermal reservoir induced stress field alteration, especially at injection and production point. Stress states, as well as pressure and temperature were compared between two models at the production grid. Input parameters are shown in Table 2. The reference stress state at the top of the reservoir was: $\tau_{xx} = 1.27e8\ Pa$, $\tau_{yy} = 0.96e8\ Pa$, $\tau_{zz} = 1.21e8\ Pa$ and all boundary conditions were constant stress condition for mechanical computation. Observation was set up at production grid and results of comparison are shown in Figure 12. The matched results validate the newly developed coupled fluid/heat flow and geomechanics model.

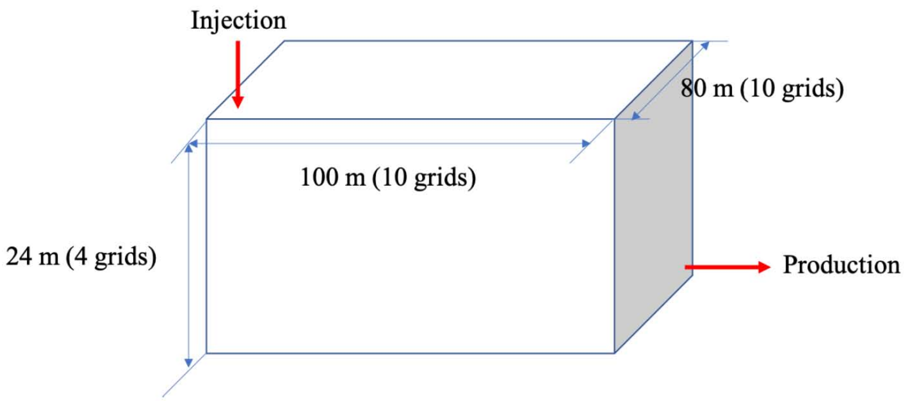

Figure 11—Geometrical small=scale model for coupled model validation (comparing TOUGH2-THM and TOUGH2-CSM)

Table 2—Input parameters for validation of coupled model (10*10*4 coarse grid model)

Parameters	Value	Unit
Matrix Permeability	2e-15	m^2
Fracture Permeability	2e-11	m^2
Initial Reservoir Pressure	4.53e7	Pa
Initial Reservoir Temperature	300	°C
Production (constant pressure)	1e7	Pa
Injection (constant rate)	0.1	kg/s
Injection specific enthalpy	3e5	J/kg
Rock/Fracture Porosity	0.05	Unitless
Rock/Fracture Heat Conductivity	5	W/(m°C)
Rock/Fracture Specific Heat	1000	J/(kg°C)
Production Well Index	4e-14	m^3
Rock Expansion Coefficient	4e-6	1/°C
Poisson's Ratio	0.25	Unitless
Young's Modulus	30	GPa
Biot's Coefficient	1	Unitless
Permeability Correlation Coefficient, c (in equation (56))	2	Unitless

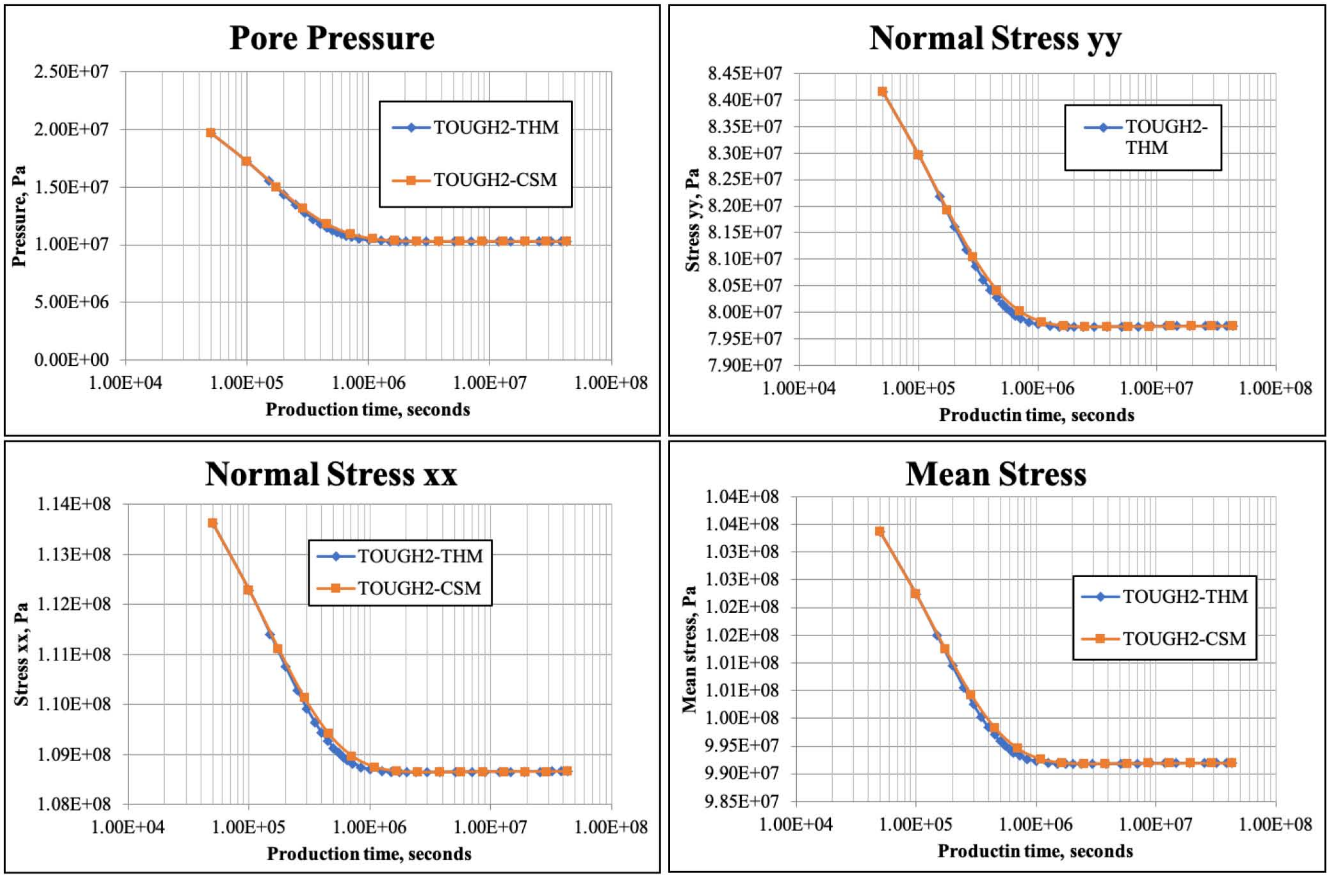

Figure 12—Comparison of pore pressure and stress state of production grid for validation case (10*10*4 coarse grid model)

Validation of TOUGH2-THM Using Analytical Solution. The well-known Mandel-Cryer problem (Mandel, 1953) describes a situation when a rectangular sample saturated with fluid subjected to a constant load at the top through a rigid plate of width 2a and the lateral boundary is allowed to drainage. Mandel-Cryer effect states that the load will be transferred to the center of the sample at the beginning period of drainage due to the rapid boundary pore pressure, resulting in a pressure increase before gradually reduced. Mandel-Cryer problem assumes plane strain, that is, no strain is allowed in y direction (perpendicular to x and z), as shown in Figure 13. Abousleiman et al. (1996) provided analytical solutions to this problem, which will be adopted here for model validation:

$$\frac{p}{p_0} = \frac{\sum_{j=1}^{\infty} \frac{sin(\xi_j)\left[cos\left(\frac{\xi_j x}{a}\right) - cos(\xi_j)\right]}{\xi_j - \sin(\xi_j)\cos(\xi_j)} exp\left(\frac{-\xi_j^2 c_v t}{a^2}\right)}{\sum_{j=1}^{\infty} \frac{sin(\xi_j)\left[cos\left(\frac{\xi_j x}{a}\right) - cos(\xi_j)\right]}{\xi_j - \sin(\xi_j)\cos(\xi_j)}} \tag{61}$$

in which ξ_j is the root of $tan(\xi) = \eta\xi$, x is the distance away from the center of the sample, and t is the time after the start of drainage. Parameter, η can be expressed as:

$$\eta = \frac{3(1-\nu)}{2(1-2\nu)} \frac{KC_f + \alpha}{\alpha} \tag{62}$$

where K is bulk modulus, α is Biot's coefficient, and C_f is the fluid compressibility. Parameter, c_v can be written as:

$$c_v = \frac{k}{\mu} \frac{1}{\frac{\phi(1+\nu)}{3K(1-\nu)} + C_f \phi} \tag{63}$$

where k is permeability and μ is fluid viscosity, and ϕ is porosity.

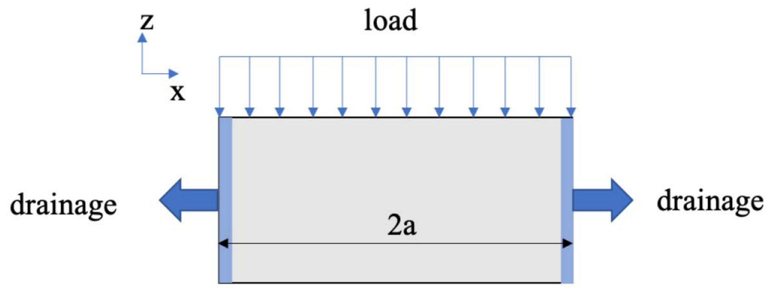

Figure 13—Geometrical model for Mandel-Cryer Problem

According to the model setup, a TOUGH-THM model was built with 51×51×1 grids, with dimensions of 1001 m × 1001 m × 10 m, indicating that $a = 500\ m$. All grids were set to be constant stress boundary with 15 MPa of y-direction normal stress and 5 MPa of mean stress at the stress load stage. All grids except top grids were boundary grids without stress flux at the drainage stage. The first simulation was modeling the pore pressure increase after the instant load was applied and the pore pressure increased to about 2.086 MPa which is consistent with analytical solution. The second simulation modeled the fluid drainage out of the sample and pore pressure in the center is observed. Input parameters are shown in Table 3. Comparison of results are shown in Figure 14.

Table 3—Input parameters of Mandel-Cryer problem for analytical solution and TOUGH2-THM

Parameters	Value	Unit
Matrix Permeability	1e-13	m^2
Initial Pore Pressure	1e5	Pa
Initial Sample Temperature	60	°C
Production (constant pressure)	1e5	Pa
Rock/Fracture Porosity	0.094	Unitless
Production Well Index	1.7e-9	m^3
Rock Expansion Coefficient	4e-6	1/°C
Poisson's Ratio	0.25	Unitless
Young's Modulus	5	GPa
Biot's Coefficient	1	Unitless
Water viscosity (@ 60°C, analytical)	0.00046	Pa-s
Water compressibility (analytical)	4.04e-10	1/Pa
Water density (analytical)	983	kg/m^3

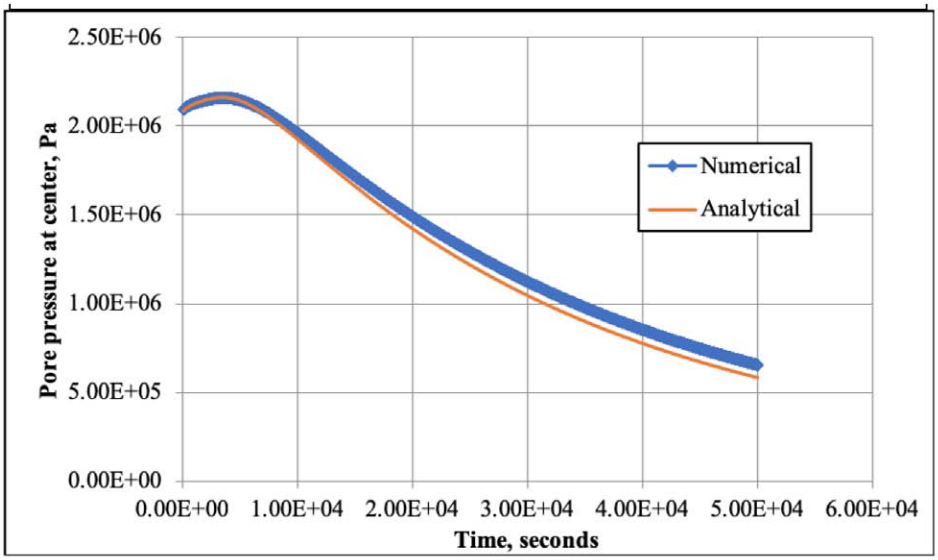

Figure 14—Comparison of pore pressure at the center for analytical and numerical solution

Application of Coupled Model for Fractured Geothermal Reservoir Simulation

After validating EDFM and TOUGH2-THM, these two models can be combined to model a geothermal reservoir development of injecting cold water for 500 days. A model with dimensions of 100 m × 100 m × 24 m was built with six long embedded discrete fractures. The geometrical mesh is shown in Figure 15, with injection and production both at fracture elements. The first step was to produce pore pressure equilibrium state. TOUGH2-THM was used without geomechanical coupling for fluid/heat flow modeling and the initial state was saved for further simulation. Afterwards, initial state was input into program for stress field initialization. Reference stress state was on the top of the reservoir: $\tau_{xx} = 1.27e8\ Pa$, $\tau_{yy} = 0.96e8\ Pa$, $\tau_{zz} = 1.21e8\ Pa$, and zero shear stresses. Reservoir boundaries were set to be constant stress boundary (using initial stress). Other reservoir input parameters are shown in Table 4.

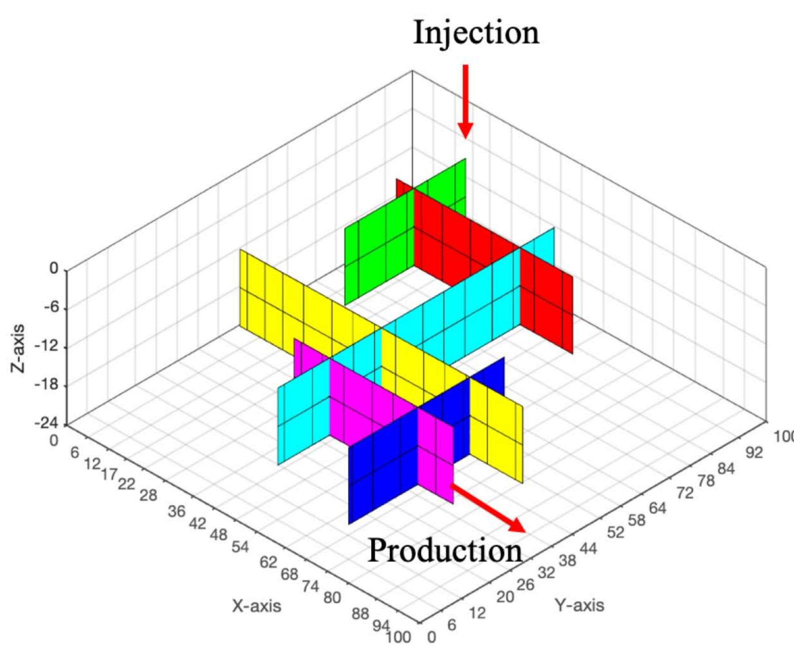

Figure 15—Geometrical model of fracture geothermal reservoir

The simulation results of pressure and temperature distribution at the depth of 12 m are shown in Figure 16. Two cases were compared: (1) fluid/heat flow model without coupling geomechanics; (2) coupled fluid/heat flow and geomechanics model. As can be seen, cold temperature isothermal contour traveled faster in geomechanical model, but reverse phenomena were observed for pressure isobar contour. This is due to the elliptic nature of the pressure equation, such that distribution of pressure change across the space is globally coupling and basically dependent on permeability: geomechanical case had a slightly lower matrix permeability due to compression but the fracture permeability was enhanced by several orders because of cold water injection. Pressure was retained to be high in no coupling case. On the other hand, temperature change relies much on convective heat flow which is equivalent to fluid transport: fluid traveled a closer distance around fracture due to reduced matrix permeability in the geomechanical case. The flow rate and production temperature out of the production well was compared in Figure 17: it is exhibited that flow rate was not much different due to the short transient period, but production temperature was lower in geomechanical case due to the enhanced fracture permeability. Production efficiency was lowered due to the temperature drop compared with non-coupling model. An observation point was placed on a fracture element near production grid and fracture permeability could be increased by two orders of magnitudes as shown in Figure 18. Normal effective stress was the dominant factor for fracture aperture before the temperature was reduced below 150 °C. Permeability is enhanced rapidly afterwards as temperature reduction kept expanding the fracture aperture.

Table 4—Input parameter for simulation of fractured geothermal reservoir

Parameters	Value	Unit
Matrix Permeability	2e-16	m^2
Fracture Permeability	2e-11	m^2
Initial Reservoir Pressure	4.53e7	Pa
Initial Reservoir Temperature	300	°C
Production (constant pressure)	1e7	Pa
Injection (constant rate)	2	kg/s
Injection specific enthalpy	3e5	J/kg
Rock/Fracture Porosity	0.05	Unitless
Rock/Fracture Heat Conductivity	5	W/(m°C)
Rock/Fracture Specific Heat	1000	J/(kg°C)
Production Well Index	4e-11	m^3
Rock Expansion Coefficient	4e-6	1/°C
Matrix/Fracture Poisson's Ratio	0.25	Unitless
Matrix Young's Modulus	30	GPa
Biot's Coefficient	1	Unitless
Matrix Permeability Correlation Coefficient, c (in equation (56))	2	Unitless
Initial Fracture Aperture	15e-6	m
Maximum Mechanical Fracture Aperture	2.5e-4	m
Fracture Permeability Correlation Coefficient, d (in equation (44))	4e-7	1/Pa

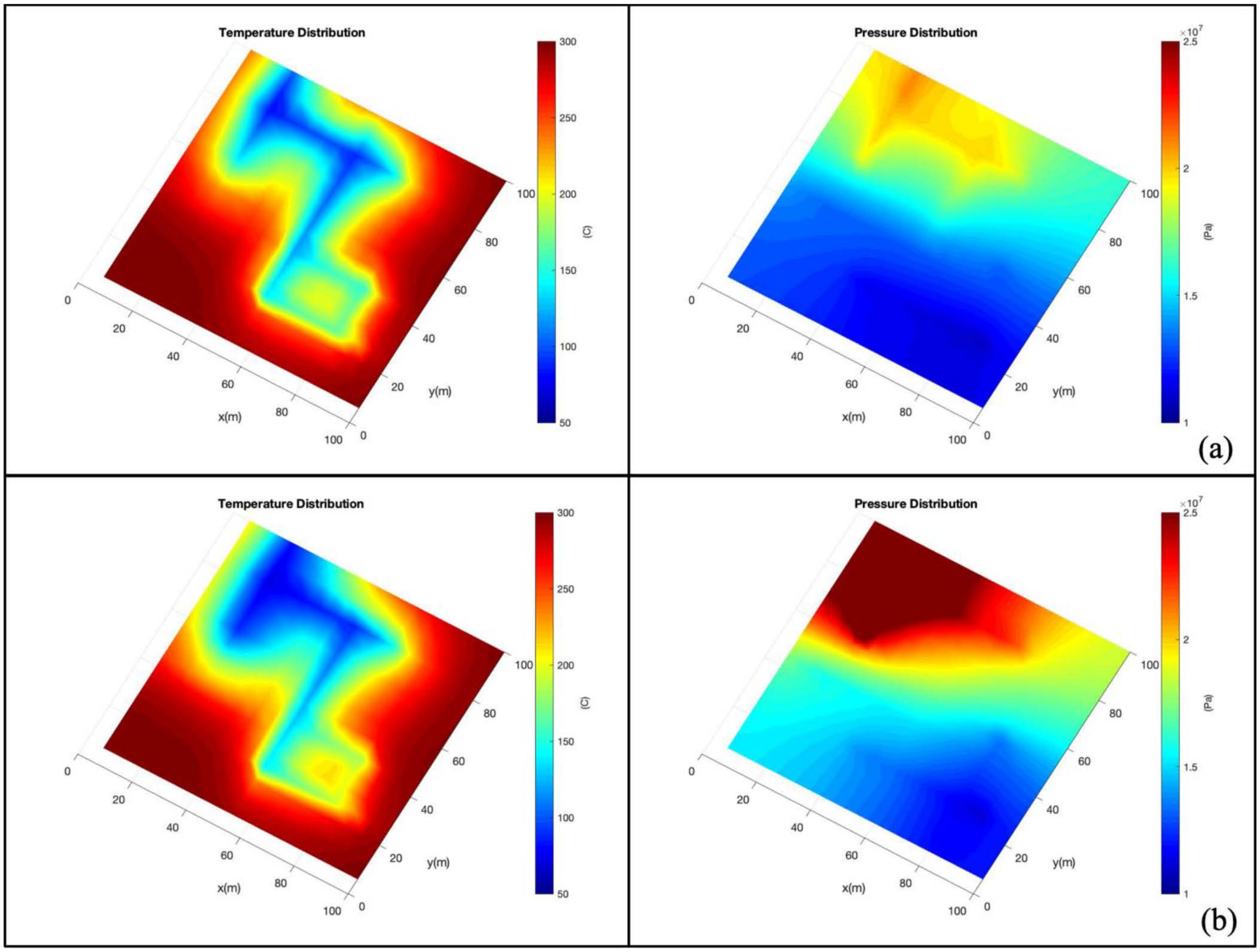

Figure 16—Temperature and pressure distribution for the fracture geothermal reservoir simulation (a) coupling geomechanics; (b) only fluid/heat flow not coupling geomechanics

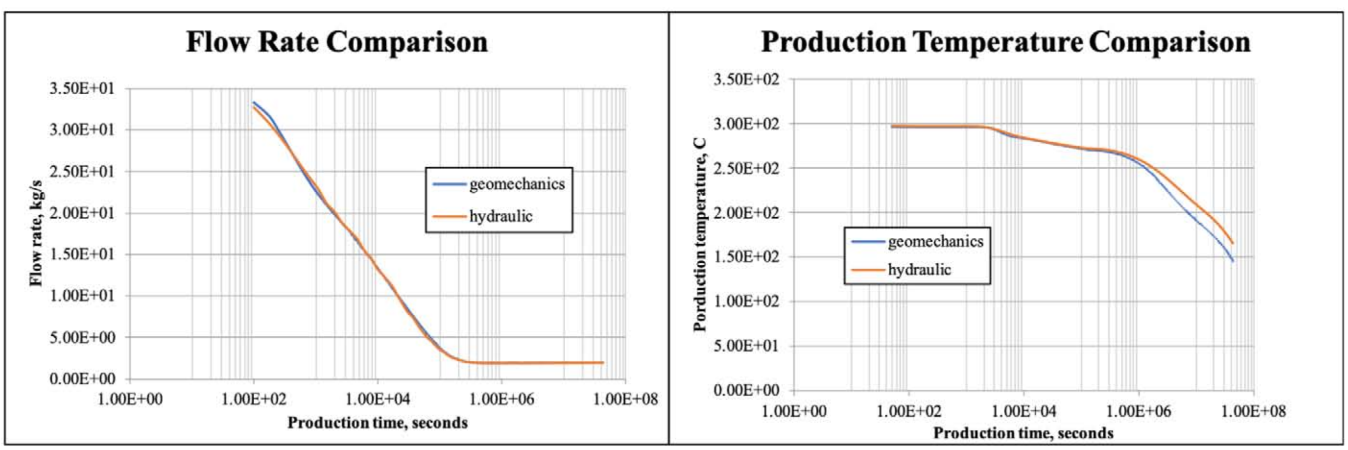

Figure 17—Comparison of flow rate and production temperature for two cases, hydraulic (no geomechanics coupling) and geomechanics (coupled model)

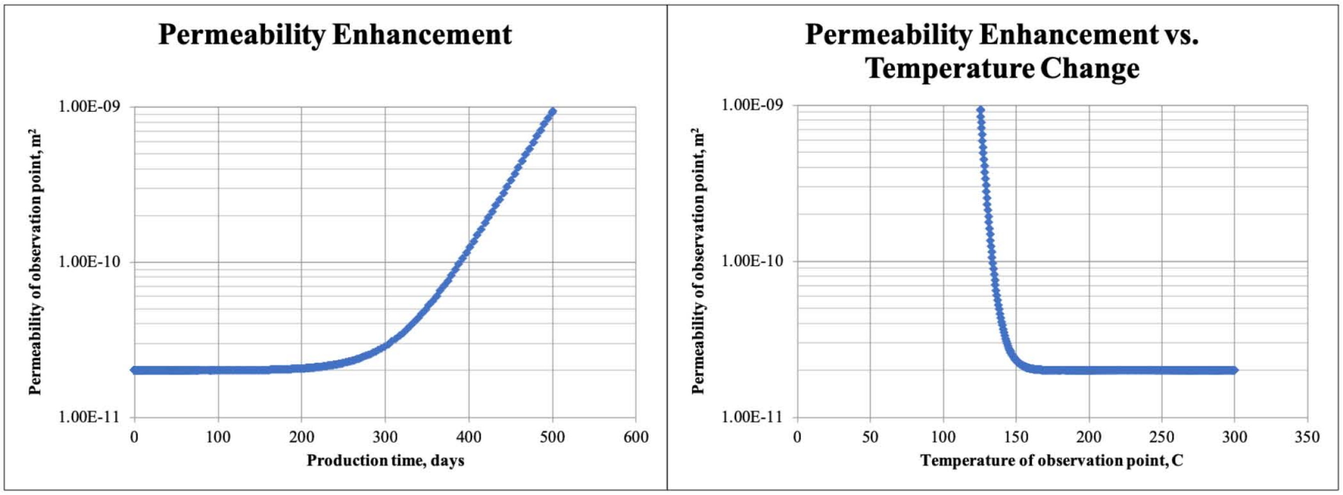

Figure 18—Permeability enhancement as temperature change and production time increases

Injection temperature was varied to observe how temperature would affect the simulation results. In the model above, injection temperature was 68 °C and in the following models, 86°C and 105 °C of water were injected into the geothermal reservoir. The simulation results of temperature distribution are shown in Figure 19. It is demonstrated that the higher injection temperature had lower effect of enhancing fracture permeability and hence the transport of cold water became slower, resulting in a less temperature alteration. It is intuitive that higher injection temperature would cause less temperature change across the reservoir, but the fracture permeability still played an essential role. At the same observation point, permeability enhancement was compared for different scenarios as well, displayed in Figure 20. Lower temperature injection significantly affected the fracture permeability, as can be observed in this result.

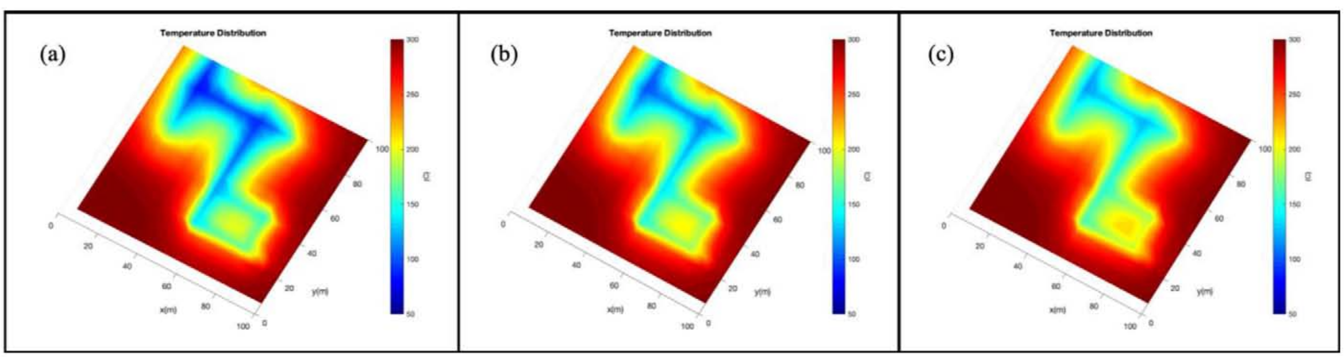

Figure 19—Temperature distribution after 500 days of injection for different injection temperatures: (a)68°C; (b)86°C; (c)105°C

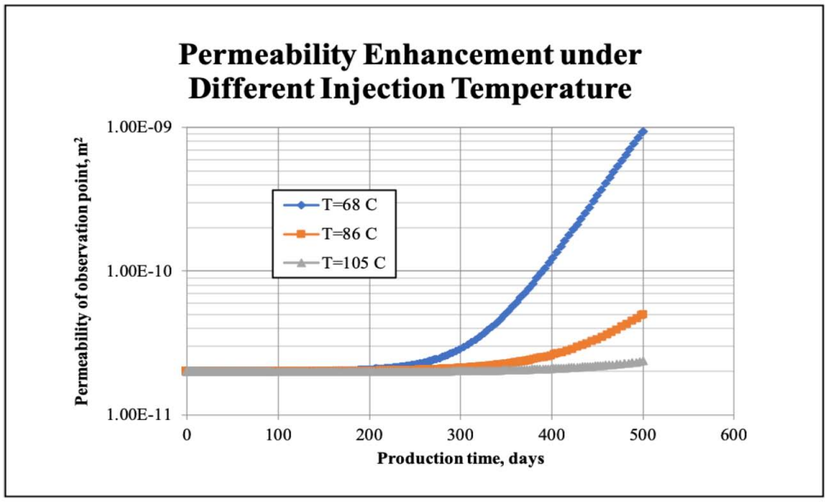

Figure 20—Observation fracture permeability enhancement under different injection temperatures

Summary and Conclusion

In this study, a new methodology was adopted to fully coupling geomechanics with fluid/heat flow for conducting geothermal reservoir modeling. This newly developed massively parallel and fully coupled model, TOUGH2-THM, selects pressure, saturation, temperature, mean stress and full stress tensor components (without z-direction normal stress) as primary variables which are all solved simultaneously during Newton's iterations. The objective of adding stress tensor components to the primary variable list is to compute normal stress exerted on embedded discrete fractures. Fractures are assumed to share the same stress state with the reservoir grid block where they are embedded. Under this assumption, normal stress on fracture surface can be calculated by stress tensor components through stress transformation in three-dimensional space. Fracture porosity and permeability then become parameters strongly sensitive to effective normal stress that could alter the fracture aperture. It is because this strong sensitivity that fully coupled model is a better choice for numerical simulation stability.

On the other hand, EDFM is modified and improved to implicitly contain all discrete fractures, no matter the fracture is within a grid block or along the block surface. A complete fracture-matrix, fracture- fracture connection list is updated using the improved version of EDFM. As a consequence, an individual fracture could have a specific response to its own stress state alteration. The geomechanics of embedded discrete fracture is highly sensitive to temperature in our model by incorporating the thermal stress on facture surface. It is assumed that temperature reduction of the fracture causes a tensile stress generated by rock matrix shrinkage. The thermal stress is in the same order of magnitude with total normal stress, which significantly influences the fracture aperture.

The modified EDFM and coupled model are both validated by existing simulation cases or analytical solutions. Then they are used to model a geothermal reservoir under cold water injection for 500 days. It can be observed that: (1) fracture is highly sensitive to temperature due to the thermal stresses; (2) geomechanical effect on fracture and rock matrix is essential to production efficiency (production temperature): temperature and pressure distribution is impacted when matrix is compressed and fracture aperture is expanded; (3) injection temperature could affect the fracture permeability by an order of magnitude with 20 °C difference and hence the fluid/heat flow process as well, so that production efficiency might be influenced.

Acknowledgement

This work was supported by Energy Modeling Group of Colorado School of Mines and Energi Simulation.

Reference

Abousleiman, Y., A. H.-D. Cheng, L. Cui, E. Detournay, and J.-C. Roegiers, 1996, *Mandel's problem revisited: Géotechnique*, v. **46**, no. 2, p. 187–195, doi:10.1680/geot.1996.46.2.187.

Barton, N., S. Bandis, and K. Bakhtar, 1985, Strength, deformation and conductivity coupling of rock joints: *International Journal of Rock Mechanics and Mining Sciences & Geomechanics Abstracts*, v. **22**, no. 3, p. 121–140, doi:10.1016/0148-9062(85)93227-9.

Chen, D., Z. Pan, and Z. Ye, 2015, Dependence of gas shale fracture permeability on effective stress and reservoir pressure: Model match and insights: Fuel, v. **139**, p. 383–392, doi:10.1016/J.FUEL.2014.09.018.

Ding, D. Y., N. Farah, B. Bourbiaux, Y.-S. Wu, and I. Mestiri, 2018, Simulation of Matrix/Fracture Interaction in Low-Permeability Fractured Unconventional Reservoirs: SPE Journal, v. **23**, no. 04, p. 1,389–1,411, doi:10.2118/182608-PA.

Garipov, T. T., M. Karimi-Fard, and H. A. Tchelepi, 2016, Discrete fracture model for coupled flow and geomechanics: Computational Geosciences, v. **20**, no. 1, p. 149–160, doi:10.1007/s10596-015-9554-z.

Gutierrez, M., R. W. Lewis, and I. Masters, 2001, Petroleum Reservoir Simulation Coupling Fluid Flow and Geomechanics: SPE Reservoir Evaluation & Engineering, v. **4**, no. 03, p. 164–172, doi:10.2118/72095-PA.

Jaeger, J. C. (John C., N. G. W. Cook, and R. W. Zimmerman, 2007, Fundamentals of rock mechanics: Blackwell Pub, 475 p.

Karimi-Fard, M., L. J. Durlofsky, and K. Aziz, 2003, An Efficient Discrete Fracture Model Applicable for General Purpose Reservoir Simulators, in SPE Reservoir Simulation Symposium: Society of Petroleum Engineers, doi:10.2118/79699-MS.

Karypis, G., and V. Kumar, 1998, A Fast and High Quality Multilevel Scheme for Partitioning Irregular Graphs: SIAM Journal on Scientific Computing, v. **20**, no. 1, p. 359–392, doi:10.1137/S1064827595287997.

Kazemi, H., 1969, Pressure Transient Analysis of Naturally Fractured Reservoirs with Uniform Fracture Distribution: Society of Petroleum Engineers Journal, v. **9**, no. 04, p. 451–462, doi:10.2118/2156-A.

Kim, J.-G., and M. D. Deo, 2000, Finite element, discrete-fracture model for multiphase flow in porous media: AIChE Journal, v. **46**, no. 6, p. 1120–1130, doi:10.1002/aic.690460604.

Kim, J., H. A. Tchelepi, and R. Juanes, 2009, Stability, Accuracy and Efficiency of Sequential Methods for Coupled Flow and Geomechanics, in SPE Reservoir Simulation Symposium: Society of Petroleum Engineers, doi:10.2118/119084-MS.

Kohl, T., K. F. Evansi, R. J. Hopkirk, and L. Rybach, 1995, Coupled hydraulic, thermal and mechanical considerations for the simulation of hot dry rock reservoirs: Geothermics, v. **24**, no. 3, p. 345–359, doi:10.1016/0375-6505(95)00013-G.

Lee, S. H., M. F. Lough, and C. L. Jensen, 2001, Hierarchical modeling of flow in naturally fractured formations with multiple length scales: Water Resources Research, v. **37**, no. 3, p. 443–455, doi:10.1029/2000WR900340.

Li, L., and S. H. Lee, 2006, Efficient Field-Scale Simulation for Black Oil in a Naturally Fractured Reservoir via Discrete Fracture Networks and Homogenized Media, in International Oil & Gas Conference and Exhibition in China: Society of Petroleum Engineers, doi:10.2118/103901-MS.

Mandel, J., 1953, Consolidation Des Sols (Étude Mathématique): *Géotechnique*, v. **3**, no. 7, p. 287–299, doi:10.1680/geot.1953.3.7.287.

McDermott, C., and O. Kolditz, 2006, Geomechanical model for fracture deformation under hydraulic, *mechanical and thermal loads: Hydrogeology Journal*, v. **14**, no. 4, p. 485–498, doi:10.1007/s10040-005-0455-4.

Min, K.-B., J. Rutqvist, C.-F. Tsang, and L. Jing, 2004, Stress-dependent permeability of fractured rock masses: a numerical study: *International Journal of Rock Mechanics and Mining Sciences*, v. **41**, no. 7, p. 1191–1210, doi:10.1016/J.IJRMMS.2004.05.005.

Minkoff, S. E., C. M. Stone, S. Bryant, M. Peszynska, and M. F. Wheeler, 2003, Coupled fluid flow and geomechanical deformation modeling: *Journal of Petroleum Science and Engineering*, v. **38**, no. 1–2, p. 37–56, doi:10.1016/S0920-4105(03)00021-4.

Moinfar, Ali, 2013, Development of an efficient embedded discrete fracture model for 3D compositional reservoir simulation in fractured reservoirs.

Moinfar, A., K. Sepehrnoori, R. T. Johns, and A. Varavei, 2013, Coupled Geomechanics and Flow Simulation for an Embedded Discrete Fracture Model, in SPE Reservoir Simulation Symposium: Society of Petroleum Engineers, doi:10.2118/163666-MS.

Pruess, K., 1983, GMINC: A Mesh Generator for Flow Simulations in Fractured Reservoirs: Berkeley.

Rutqvist, J., 2011, Status of the TOUGH-FLAC simulator and recent applications related to coupled fluid flow and crustal deformations: *Computers & Geosciences*, v. **37**, no. 6, p. 739–750, doi:10.1016/J.CAGEO.2010.08.006.

Rutqvist, J., Y.-S. Wu, C.-F. Tsang, and G. Bodvarsson, 2002, A modeling approach for analysis of coupled multiphase fluid flow, heat transfer, and deformation in fractured porous rock: *International Journal of Rock Mechanics and Mining Sciences*, v. **39**, no. 4, p. 429–442, doi:10.1016/S1365-1609(02)00022-9.

Settari, A., and D. A. Walters, 2001, Advances in Coupled Geomechanical and Reservoir Modeling With Applications to Reservoir Compaction: *SPE Journal*, v. **6**, no. 03, p. 334–342, doi:10.2118/74142-PA.

Taron, J., and D. Elsworth, 2010, Coupled mechanical and chemical processes in engineered geothermal reservoirs with dynamic permeability: *International Journal of Rock Mechanics and Mining Sciences*, v. **47**, no. 8, p. 1339–1348, doi:10.1016/J.IJRMMS.2010.08.021.

Taron, J., and D. Elsworth, 2009, Thermal–hydrologic–mechanical–chemical processes in the evolution of engineered geothermal reservoirs: International Journal of Rock Mechanics and Mining Sciences, v. **46**, no. 5, p. 855–864, doi:10.1016/J.IJRMMS.2009.01.007.

Verruijt, A., 2013, Theory and problems of poroelasticity: *Delft University of Technology*.

Wang, C., 2018a, A multi-scale, multi-continuum and multi-physics model to simulate coupled fluid flow and geomechanics in shale gas reservoirs.

Wang, C., 2018b, A multi-scale, multi-continuum and multi-physics model to simulate coupled fluid flow and geomechanics in shale gas reservoirs.

Wang, S., Z. Huang, Y.-S. Wu, P. H. Winterfeld, and L. E. Zerpa, 2016, A semi-analytical correlation of thermal-hydraulic-mechanical behavior of fractures and its application to modeling reservoir scale cold water injection problems in enhanced geothermal reservoirs: *Geothermics*, v. **64**, p. 81–95, doi:10.1016/J.GEOTHERMICS.2016.04.005.

Wang, C., Y.-S. Wu, Y. Xiong, P. H. Winterfeld, and Z. Huang, 2015, Geomechanics Coupling Simulation of Fracture Closure and Its Influence on Gas Production in Shale Gas Reservoirs, in SPE Reservoir Simulation Symposium: Society of Petroleum Engineers, doi:10.2118/173222-MS.

Wang, S., J. Zhang, Z. Yang, C. Yin, Y. Wang, R. Zhang, P. Winterfeld, and Y.-S. Wu, 2017, Fully Coupled Thermal-Hydraulic-Mechanical Reservoir Simulation with Non-Isothermal Multiphase Compositional Modeling, in SPE Reservoir Simulation Conference: Society of Petroleum Engineers, doi:10.2118/182595-MS.

Warren, J. E., and P. J. Root, 1963, The Behavior of Naturally Fractured Reservoirs: *Society of Petroleum Engineers Journal*, v. **3**, no. 03, p. 245–255, doi:10.2118/426-PA.

Winterfeld, P. H., and Y.-S. Wu, 2016, Simulation of Coupled Thermal/Hydrological/Mechanical Phenomena in Porous Media: *SPE Journal*, v. **21**, no. 03, p. 1041–1049, doi:10.2118/173210-PA.

Wu, Y.-S., 2000, On the effective continuum method for modeling multiphase flow, multicomponent transport, and heat transfer in fractured rock: *American Geophysical Union (AGU)*, p. 299–312, doi:10.1029/GM122p0299.

Wu, Y.-S., H. H. Liu, and G. S. Bodvarsson, 2004, A triple-continuum approach for modeling flow and transport processes in fractured rock: *Journal of Contaminant Hydrology*, v. **73**, no. 1–4, p. 145–179, doi:10.1016/J.JCONHYD.2004.01.002.

Xiong, Y., P. Fakcharoenphol, P. Winterfeld, R. Zhang, and Y.-S. Wu, 2013, Coupled Geomechanical and Reactive Geochemical Model for Fluid and Heat Flow: Application for Enhanced Geothermal Reservoir, in SPE Reservoir Characterization and Simulation Conference and Exhibition: Society of Petroleum Engineers, doi:10.2118/165982-MS.

Xiong, Y., P. Winterfeld, C. Wang, Z. Huang, and Y.-S. Wu, 2015, Effect of Large Capillary Pressure on Fluid Flow and Transport in Stress-sensitive Tight Oil Reservoirs, in SPE Annual Technical Conference and Exhibition: Society of Petroleum Engineers, doi:10.2118/175074-MS.

Xu, Y., J. S. A. Cavalcante Filho, W. Yu, and K. Sepehrnoori, 2017, Discrete-Fracture Modeling of Complex Hydraulic-Fracture Geometries in Reservoir Simulators: *SPE Reservoir Evaluation & Engineering*, v. **20**, no. 02, p. 403–422, doi:10.2118/183647-PA.

Zhang, K., Y. S. Wu, C. Ding, K. Pruess, and E. Elmroth, 2001, Parallel Computing Techniques for Large-Scale Reservoir Simulation of Multi-Component and Multiphase Fluid Flow, in SPE Reservoir Simulation Symposium: Society of Petroleum Engineers, doi:10.2118/66343-MS.

Zhang, R., X. Yin, P. H. Winterfeld, and Y.-S. Wu, 2016, A fully coupled thermal-hydrological mechanical-chemical model for CO2 geological sequestration: *Journal of Natural Gas Science and Engineering*, v. **28**, p. 280–304, doi:10.1016/J.JNGSE.2015.11.037.